

Article

Prograde and Retrograde Terms of Gravimetric Polar Motion Excitation Estimates from the GRACE Monthly Gravity Field Models

Jolanta Nastula  and Justyna Śliwińska * 

Space Research Centre, Polish Academy of Sciences, 00-716 Warsaw, Poland; nastula@cbk.waw.pl

* Correspondence: jsliwinska@cbk.waw.pl

Received: 22 October 2019; Accepted: 21 December 2019; Published: 1 January 2020



Abstract: From 2002 to 2017, the Gravity Recovery and Climate Experiment (GRACE) mission's twin satellites measured variations in the mass redistribution of Earth's superficial fluids, which disturb polar motion (PM). In this study, the PM excitation estimates were computed from two recent releases of GRACE monthly gravity field models, RL05 and RL06, and converted into prograde and retrograde circular terms by applying the complex Fourier transform. This is the first such analysis of circular parts in GRACE-based excitations. The obtained series were validated by comparison with the residuals of observed polar motion excitation (geodetic angular momentum (GAM)–atmospheric angular momentum (AAM)–oceanic angular momentum (OAM) (GAO)) determined from precise geodetic measurements of the pole coordinates. We examined temporal variations of hydrological excitation function series (or hydrological angular momentum, HAM) in four spectral bands: seasonal, non-seasonal, non-seasonal short-term, and non-seasonal long-term. The general conclusions arising from the conducted analyses of prograde and retrograde terms were consistent with the findings from the equatorial components of PM excitation studies drawn in previous research. In particular, we showed that the new GRACE RL06 data increased the consistency between different solutions and improved the agreement between GRACE-based excitation series and reference data. The level of agreement between HAM and GAO was dependent on the oscillation considered and was higher for long-term than short-term variations. For most of the oscillations considered, the highest agreement with GAO was obtained for CSR RL06 and ITSG-Grace2018 solutions. This study revealed that both prograde and retrograde circular terms of PM excitation can be determined by GRACE with similar levels of accuracy. The findings from this study may help in choosing the most appropriate GRACE solution for PM investigations and can be useful in future improvements to GRACE data processing.

Keywords: GRACE; Earth rotation; polar motion excitation; complex Fourier transform

1. Introduction

Polar motion (PM) is disturbed by many processes with diverse temporal variability ranging from several days to many decades [1]. For time scales of a few years or less, the major contributors to changes in PM are angular momentum changes induced by mass redistribution of Earth's surficial fluids (atmosphere, ocean, and land hydrosphere). These contributions are described as PM excitation functions or angular momentum functions, namely atmospheric angular momentum (AAM), oceanic angular momentum (OAM), and hydrological angular momentum (HAM), and can be determined with several geophysical models. However, while the role of AAM and OAM has been extensively investigated [2–8], the main source of uncertainties in PM excitation is HAM.

HAM estimates obtained from different hydrological and climate models exhibit visible discrepancies, both with respect to each other and with respect to the reference hydrological signal

in observed PM excitation, derived from precise geodetic measurements [9–15]. The main reason for the discrepancies between estimations of HAM by different models is the differences in meteorological model forcing data, processing algorithms, temporal and spatial resolution, and the number of parameters estimated [16]. Disagreement with observed PM data is caused by the lack of accounting for some water storage components within the model or unrealistic simulations of other variables. In addition, other geophysical effects, such as earthquake-induced co- and post-seismic deformations [17] or Earth's core–mantle coupling [18], are usually not considered by models in a rigorous way.

As an alternative to the use of hydrological models, PM excitation can be obtained from observations of temporal variations in the gravity field that are caused by changes in the Earth's mass redistribution. Such data were provided by the Gravity Recovery and Climate Experiment (GRACE) mission between 2002 and 2017 [19]. The high-precision observations of global mass change are being continued thanks to the May 2018 launch of the successor of the mission, GRACE Follow-On. The so-called GRACE Level 2 data (or GRACE satellite-only model; GSM), having a form of spherical harmonics coefficients of Earth's geopotential (or Stokes coefficients), can be used for designation of mass-related PM excitation. The variations of degree-2, order-1 coefficients (ΔC_{21} , ΔS_{21}) are proportional to the equatorial components (χ_1 , χ_2) of the PM excitation [20]. After reducing GRACE-based excitations by tidal contributions (atmospheric tides, ocean tides, pole tides, and solid Earth tides), as well as non-tidal atmospheric and oceanic impacts, the remaining signal indicates the land hydrosphere effects with barystatic sea-level contributions [21] and earthquake signals [22] retained. Such PM excitation functions have been variously named in previous research: gravimetric excitation functions, gravimetric–hydrological excitation functions, GRACE-based HAM functions, or GSM-based angular momentum (GSMAM) functions.

Recently, new GRACE solutions (RL06) have been developed and made available to the scientific community by the official GRACE data centres at the Center for Space Research (CSR) in Austin, USA; Jet Propulsion Laboratory (JPL) in Pasadena, USA; and GeoForschungsZentrum (GFZ) in Potsdam, Germany. However, at the same time, other data centres also joined the network, for example, Institute of Theoretical Geodesy and Satellite Geodesy (ITSG) of the Graz University of Technology in Austria released their ITSG-Grace2018 series, and the Centre National d'Etudes Spatiales/Groupe de Recherche de Géodésie Spatiale (CNES/GRGS) in France processed the CNES/GRGS RL04 solution. The first attempts to validate these solutions with respect to the observed PM excitation have been made in recent works [23–25]. These studies have all shown that both the consistency between particular solutions and the agreement with reference data have increased when applying the newly processed GRACE data. However, full agreement between GRACE-based and observed hydrological excitation has not yet been achieved.

The PM excitation is commonly described using either the two equatorial components of PM excitation function, χ_1 (along the Greenwich Meridian) and χ_2 (along 90°E), or their complex form ($\chi_1 + i\chi_2$). However, it is well known that PM excitation exhibits two circular terms: χ_R (retrograde or clockwise) and χ_P (prograde or counter-clockwise). In previous research, Earth's PM excitation was generally decomposed into χ_P and χ_R terms, but at one fixed frequency; seasonal oscillations (annual, semi-annual, or ter-annual) were usually the main focus, and χ_P and χ_R terms of seasonal variations were represented by amplitudes and phases of annual, semi-annual, and ter-annual oscillations [1,3,9,11–15,26–28]. Previous studies [1,28] have shown that annual geodetic excitation, derived from precise measurements of pole coordinates, has an elliptic character with the semi-major axis of longitude 80°–90°E and a stable ellipticity.

The first attempt to investigate the prograde and retrograde terms of PM excitation independently from the frequency was undertaken by the authors of [29]. The circular terms of geophysical PM excitations derived from different atmosphere, ocean, and land hydrosphere models were reconstructed in the time domain by the author. The time series of χ_P and χ_R obtained in this way were then compared with the corresponding estimates computed from geodetic observations. The author aimed to prove a

dependence between the χ_P and χ_R parts of PM excitation in the spectral and time domains, and found a visible correlation between them.

In this paper, we extend this type of PM excitation analysis, by evaluating GRACE-based HAM functions. We reconstructed total prograde and retrograde terms of gravimetric HAM in the time domain from χ_1 and χ_2 equatorial components, using the complex Fourier transform (CFT) [30]. This is the first study to analyse the GRACE excitation data in this manner. The circular terms of investigated series were then separated into seasonal and non-seasonal parts and the latter were filtered to separately assess long-term and short-term variations. Our objective was to validate these oscillations in χ_P and χ_R terms of gravimetric–hydrological excitation functions using geodetically observed PM excitation. The focus was to consider what the new GRACE RL06 solutions might contribute to the understanding of residual PM excitations as observed by space geodetic techniques. On the basis of the comparison with a data series from a previous GRACE release (RL05), we aimed to determine the scale of the improvement in correlation and variance agreement between gravimetric–hydrological and observed PM excitation functions. By comparing our results with those obtained from the analyses of χ_1 and χ_2 components of PM excitation from previous works, we aimed to assess whether a different representation method produces similar findings. In particular, we attempted to indicate the GRACE solutions that best matched the geodetic observations of PM for seasonal and non-seasonal oscillations, and compared these designations with results obtained from previously published analyses of equatorial PM excitation components. The results of this study could be used to recommend the GRACE solutions that are most appropriate for PM excitation determination on certain oscillations. Furthermore, our attempt to quantify the size of increase in consistency between new GRACE series and geodetic observations of PM may be useful in future improvements to GRACE and GRACE Follow-On data processing.

2. Data

2.1. Reference Series

The χ_1 , χ_2 equatorial components of the observed geodetic PM excitation function (GAM) can be computed from observed coordinates (x, y) of the Earth's pole by solving Liouville's equation [31,32]. The pole coordinates are routinely delivered as daily C04 series of Earth orientation parameters (EOP), derived from the combination of very long baseline interferometry (VLBI), satellite laser ranging (SLR), and global navigation satellite systems (GNSS) space geodesy techniques. The newest version of EOP data, EOP 14 C04 [33], is fully consistent with the International Terrestrial Reference Frame 2014 (ITRF 2014) [34], provided by the International Earth Rotation and Reference System Service (IERS) (<https://www.iers.org/>), and updated on a regular basis with monthly latency.

To separate hydrology-related effects from observed GAM, the impacts of atmosphere and ocean (described by AAM and OAM functions, respectively) were removed using geophysical models:

$$GAO = GAM - (AAM_{mass} + AAM_{motion} + OAM_{mass} + OAM_{motion}), \quad (1)$$

where AAM_{mass} represents the impact of atmospheric pressure, AAM_{motion} represents the impact of zonal wind speed, OAM_{mass} represents the impact of ocean bottom pressure, and OAM_{motion} represents the impact of ocean currents.

The residual signal series obtained from Equation 1 are often denoted as geodetic residuals, GAM–AAM–OAM or simply GAO. They mainly reflect the impact of the land hydrosphere on PM excitation, but also some other effects, including barystatic sea-level changes owing to the inflow of water from land into the oceans (sea-level angular momentum, SLAM) [35], tectonic signals from large earthquakes [36,37], or signatures of geomagnetic jerks [38].

In this study, we used the following datasets to compute GAO:

- GAM: χ_1 and χ_2 components of observed geodetic PM excitations, obtained from the EOP 14 C04, were taken from the IERS website (<https://www.iers.org/>).
- AAM_{mass} + OAM_{mass}: we computed χ_1 and χ_2 components of joint AAM plus OAM mass terms from ΔC_{21} , ΔS_{21} coefficients of the GRACE average non-tidal atmosphere and ocean de-aliasing time series GAC JPL RL06, by applying the formulas shown in Section 3 (Equations (2) and (3)). The GAC data have the form of monthly time series of spherical harmonic coefficients with a maximum degree and order of 180. They represent anomalous contributions of the non-tidal atmospheric surface and dynamic ocean pressure variations, and upper-air density anomalies [39,40]. The GAC RL06 time series are consistent with GRACE AOD1B RL06 (GRACE Atmosphere and Ocean De-Aliasing Level 1B Release 6 [39,40]). The data were accessed from <https://podaac-tools.jpl.nasa.gov/drive/files/allData/grace/L2/JPL/RL06>.
- AAM_{motion}: χ_1 and χ_2 components for the motion term of AAM were provided by the GFZ and accessed from <ftp://esmdata.gfz-potsdam.de/./EAM/>. They were computed from the European Centre for Medium-Range Weather Forecasts (ECMWF) operational atmospheric model [26]. The current AAM version provided by GFZ is consistent with GRACE AOD1B RL06.
- OAM_{motion}: χ_1 and χ_2 components for the motion term of OAM were provided by GFZ and accessed from <ftp://esmdata.gfz-potsdam.de/./EAM/>. They were computed from the Max Planck Institute Ocean Model (MPIOM) [41] and forced with ECMWF atmospheric data. The current OAM version provided by GFZ is consistent with GRACE AOD1B RL06.

2.2. Evaluated Series

2.2.1. GRACE Level 2 Data

The PM excitation series evaluated here were computed from monthly GRACE satellite-only models (GSM), also denoted as GRACE Level 2 data. To do so, we converted ΔC_{21} , ΔS_{21} coefficients of the geopotential into χ_1 and χ_2 equatorial components of mass-related PM excitation function (see Section 3). In the GSM coefficients of Earth's geopotential, the non-tidal atmospheric and oceanic impacts, associated with AOD1B product (or its spherical harmonic representation, GAC), are removed. Consequently, the resulting excitation functions describe the effects from terrestrial water storage with SLAM, glacial isostatic adjustment (GIA), tectonic signals, or geomagnetic jerks remaining. It is well known that GIA has a non-negligible impact on polar motion excitation trends. This signal is contained in both GRACE data and GAO. We eliminated this effect from all time series by removing trends, because they are out of the scope of this paper.

In this paper, we evaluated gravimetric PM excitation functions calculated from the following GRACE GSM fields provided by five different processing centres:

- CSR, Austin, USA—CSR RL05 [42] and CSR RL06 [43] solutions;
- JPL, Pasadena, USA—JPL RL05 [44] and JPL RL06 [45] solution;
- GFZ, Potsdam, Germany—GFZ RL05 [46] and GFZ RL06 [47] solutions;
- CNES/GRGS, Toulouse, France—CNES/GRGS RL03 [48] and CNES/GRGS RL04 [49] solutions;
- ITSG, Graz University of Technology, Austria—ITSG-Grace2016 [50] and ITSG-Grace2018 [51] solutions.

The time series were accessed from: PO.DAAC Drive (<https://podaac-tools.jpl.nasa.gov/drive/files/GeodeticsGravity/grace/L2>) for data processed by the official GRACE data centres at CSR, JPL, and GFZ; from Graz University of Technology data server (<http://ftp.tugraz.at/outgoing/ITSG/GRACE/ITSG-Grace2018/monthly/>) for ITSG-Grace2016 and ITSG-Grace2018 solutions; and from the CNES/GRGS website (<https://grace.obs-mip.fr/>) for CNES/GRGS RL03 and CNES/GRGS RL04 solutions.

It should be noted that ITSG-Grace2016 and CNES/GRGS RL03 solutions were specifically designed to be compatible with official RL05 solutions from CSR, JPL, and GFZ, while ITSG-Grace2018 and CNES/GRGS RL04 were designed to correspond to official CSR RL06, JPL RL06, and GFZ RL06 solutions.

Therefore, we used the RL05 designation for all five older solutions. Consequently, RL06 generation includes CSR RL06, JPL RL06, GFZ RL06, CNES/GRGS RL04, and ITSG-Grace2018 throughout the remainder of this paper.

2.2.2. HAM and SLAM Functions Processed by GFZ

For comparison with GRACE-based excitations, we also consider HAM computed from the land surface discharge model (LSDM) and made available by GFZ (<ftp://esmdata.gfz-potsdam.de/./EAM/>). The LSDM, given at $0.5^\circ \times 0.5^\circ$ spatial resolution and 24 h temporal resolution, provides simulations of lateral and vertical water transport and water storage on continents [52,53]. The model is forced with precipitation, evaporation, and temperature from the ECMWF operational atmospheric data. The χ_1 , χ_2 LSDM-based hydrological excitation functions were taken directly from the GFZ website (<ftp://esmdata.gfz-potsdam.de/./EAM/>).

At this point, it should be reminded that both GRACE models and GAM (as well as GAO, which was computed after removing AAM and OAM from GAM) include barystatic sea level changes due to inflow of water from lands into the oceans (described by sea-level angular momentum SLAM). However, SLAM is not included in hydrological models that provide the data from lands only. Therefore, to make LSDM-based HAM more comparable with GAO and GRACE estimates, we added SLAM to it. The SLAM series considered here, available in the form of χ_1 , χ_2 , were based on ECMWF and LSDM data, and provided by the GFZ (<ftp://esmdata.gfz-potsdam.de/./EAM/>) [54,55]. Therefore, GAO, GRACE-based HAM, and LSDM-based HAM considered here should be consistent in the sense that each of them include SLAM. In the following, the HAM obtained from LSDM with SLAM added is simply called LSDM.

3. Methods

3.1. Time-Series Processing

The equatorial components of gravimetric–hydrological PM excitation function were computed from ΔC_{21} , ΔS_{21} coefficients of the geopotential using the following formula (based on the work of [32] and Chapter 3.09.5 in the work of [20]):

$$\begin{aligned}\chi_1 &= -\sqrt{\frac{5}{3}} \cdot \frac{1.608 \cdot R_e^2 \cdot M}{C - A'} \Delta C_{21}, \\ \chi_2 &= -\sqrt{\frac{5}{3}} \cdot \frac{1.608 \cdot R_e^2 \cdot M}{C - A'} \Delta S_{21},\end{aligned}\quad (2)$$

where R_e and M are the Earth's mean Earth's radius (6378136.6 m) and mass (5.9737×10^{24} kg), respectively; $A = 8.0101 \times 10^{37}$ kg·m², $B = 8.0103 \times 10^{37}$ kg·m², and $C = 8.0365 \times 10^{37}$ kg·m² are the principal moments of inertia for Earth; $A' = (A + B)/2$ is an average of the equatorial principal moments of inertia; and ΔC_{21} and ΔS_{21} are the spherical harmonics coefficients of the gravity field (Table 1 in [20]).

All PM excitation series considered here (GAO, HAM computed from LSDM and GRACE-based HAM) were processed in the following manner:

1. All series were down-sampled to monthly time steps using a Gaussian filter because of the different sampling resolutions of the data sources (3 h for ECMWF and MPIOM models; 24 h for GAM, SLAM, and HAM from LSDM; and only monthly for GRACE GSM and GAC).
2. The linear trends and seasonal signals were estimated together using the least squares methods, by fitting the model comprising of the first degree polynomial and the sum of sinusoids with the periods of 1, 1/2, and 1/3 year. Then, to analyse seasonal variations, we removed the trends. It should be noted that removing of trends allowed to effectively eliminate GIA. The trends in GAO and HAM are out of the scope of this paper.

3. The non-seasonal changes were obtained after removing linear trends and seasonal variations from the series.
4. The prograde and retrograde terms (χ_P , χ_R) of the PM excitation function (seasonal and non-seasonal separately) were computed using the CFT method [29] (see Section 3.2).
5. The non-seasonal prograde and retrograde terms of PM excitation function were separated into short-term (<730 days) and long-term (>730 days) oscillations using a higher-order eight-pole sine wave Butterworth filter [56].

In the study, we considered the same period for all data sets, namely between January 2003 and December 2015.

3.2. Complex Fourier Transform

Over a given time interval, the complex equatorial components of PM excitation can be decomposed into a complex Fourier series as follows [29]:

$$\chi(t) = \sum_{\sigma > 0} a_{\sigma}^{+} e^{i\sigma t} + \sum_{\sigma > 0} a_{\sigma}^{-} e^{-i\sigma t} + \chi_0, \quad (3)$$

where a_{σ}^{+} is the complex amplitude of the prograde term of angular frequency σ , a_{σ}^{-} is the complex amplitude of retrograde term of the same frequency, χ_0 is a constant term, and i is an imaginary unit.

In time domain, prograde and retrograde PM excitation terms at a given frequency can be determined by the following:

$$\begin{aligned} \chi_{\sigma}^{+}(t) &= a_{\sigma}^{+} e^{i\sigma t} = A_{\sigma}^{+} e^{i\Phi_{\sigma}^{+}} e^{i\sigma t}, \\ \chi_{\sigma}^{-}(t) &= a_{\sigma}^{-} e^{-i\sigma t} = A_{\sigma}^{-} e^{i\Phi_{\sigma}^{-}} e^{-i\sigma t}, \end{aligned} \quad (4)$$

where A_{σ}^{+} and A_{σ}^{-} express amplitudes, and Φ_{σ}^{+} and Φ_{σ}^{-} express phases.

The total prograde and retrograde components of PM excitation function in time domain can be obtained by adding the individual frequency terms of the Fourier decomposition:

$$\begin{aligned} \chi^{+}(t) &= \sum_{\sigma > 0} a_{\sigma}^{+} e^{i\sigma t}, \\ \chi^{-}(t) &= \sum_{\sigma > 0} a_{\sigma}^{-} e^{-i\sigma t}. \end{aligned} \quad (5)$$

4. Results

Our results comprise time series comparison (Section 4.1) and the study of agreement between HAM and GAO, which included correlation, relative explained variance, and coefficients of determination analysis (Section 4.2). We analysed the following oscillations in PM variation: seasonal (sum of annual, semi-annual, and ter-annual changes), non-seasonal, non-seasonal short (<730 days), and non-seasonal long (>730 days).

4.1. Time-Series Comparison

Figure 1 presents retrograde and prograde seasonal terms of GAO and HAM computed from different GRACE solutions and the hydrological LSDM. The χ_P and χ_R parts reveal similar amplitudes within each GRACE solution; however, for GAO and the LSDM-based HAM, χ_R terms exhibited visibly stronger amplitudes than those observed for χ_P terms. With the new GRACE solutions, only the JPL and GFZ series revealed a reduction in amplitudes, whereas very little amplitude change was detected for other GRACE data. This was also revealed by the standard deviation (STD) values (see Table A1 in the Appendix A). Notably, a reduction of STD for both χ_P and χ_R was observed for JPL and GFZ, whereas we noted an increase in this parameter for other solutions. Figure 2 compares the mean χ_P and χ_R values with ranges between minimum and maximum for the RL05 and RL06 solutions. Updating

some background models and processing algorithms in the GRACE RL06 data resulted in increased compliance of HAM between individual solutions (indicated by reduced range), especially for the χ_R term. However, there was still no full agreement between GAO and mean HAM obtained from the GRACE observations. In particular, the χ_R part for the GRACE-based mean HAM data clearly underestimated seasonal variations of both GAO and LSDM-based HAM.

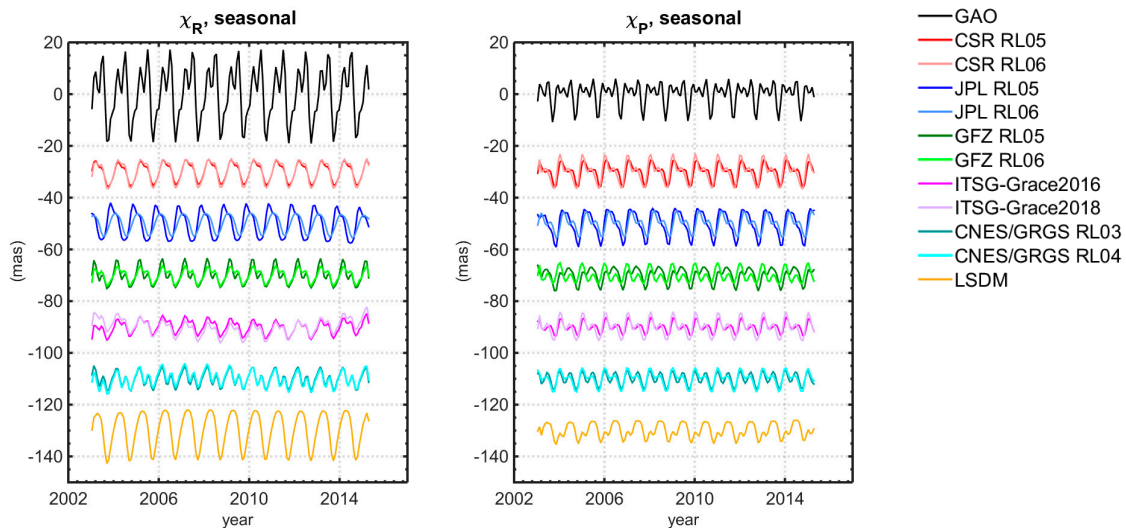


Figure 1. Retrograde and prograde parts (χ_R and χ_P , respectively) of seasonal variation in geodetic angular momentum (GAM)–atmospheric angular momentum (AAM)–oceanic angular momentum (OAM) (GAO), in hydrological angular momentum (HAM) computed from different Gravity Recovery and Climate Experiment (GRACE) solutions, and HAM from the land surface discharge model (LSDM). The units are milliseconds of arc (mas). For better visibility, a bias was added to various HAM in order to shift them relative to each other. ITSG, Institute of Theoretical Geodesy and Satellite Geodesy; GFZ, GeoForschungsZentrum; CSR, Centre for Space Research; JPL, Jet Propulsion Laboratory; CNES/GRGS, Centre National d’Etudes Spatiales/Groupe de Recherche de G eod esie Spatiale.

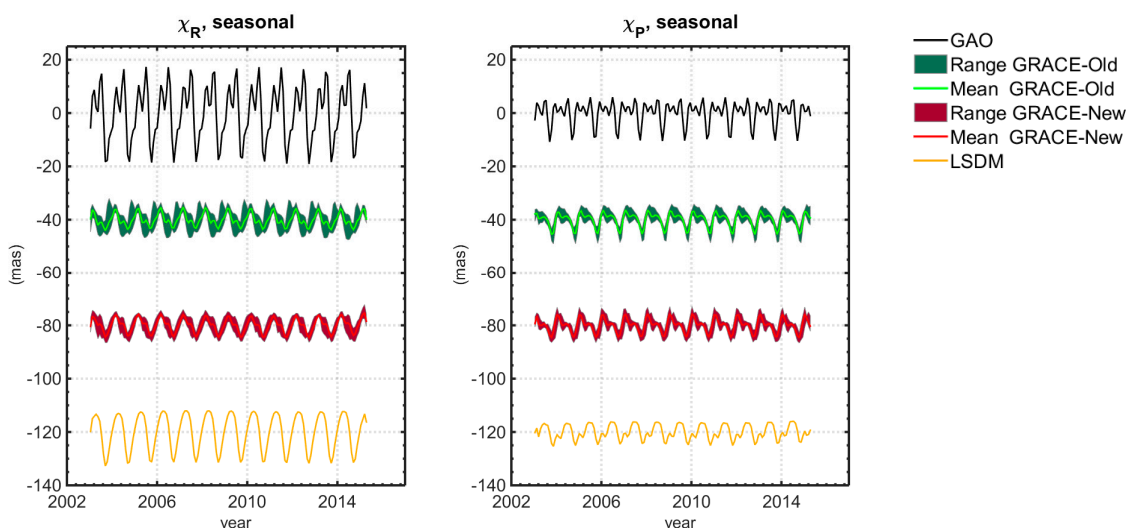


Figure 2. Comparison of mean value with ranges between minimum and maximum for χ_R and χ_P of seasonal variation in HAM for the old and new GRACE solutions. Time series of GAO and HAM from the LSDM are provided for comparison. The units are milliseconds of arc (mas). For better visibility, a bias was added to various HAM in order to shift them relative to each other.

The χ_R and χ_P parts of non-seasonal oscillations in GAO and HAM are shown in Figure 3. The χ_R circular term in non-seasonal variation appeared to be stronger than the χ_P term for most of the old

GRACE HAM series, as indicated by the STD values presented in Table A1. However, this was not apparent for GAO and HAM computed from the new GRACE solutions and the LSDM. The comparison of the mean χ_P and χ_R non-seasonal changes with ranges between minimum and maximum (Figure 4) showed that with the new GRACE RL06 solutions, different estimations of HAM were more similar; however, visible discrepancies were still present. Nevertheless, the HAM from the mean of all new GRACE solutions seemed to be more consistent with GAO and LSDM-based HAM than the HAM from any single GRACE solution.

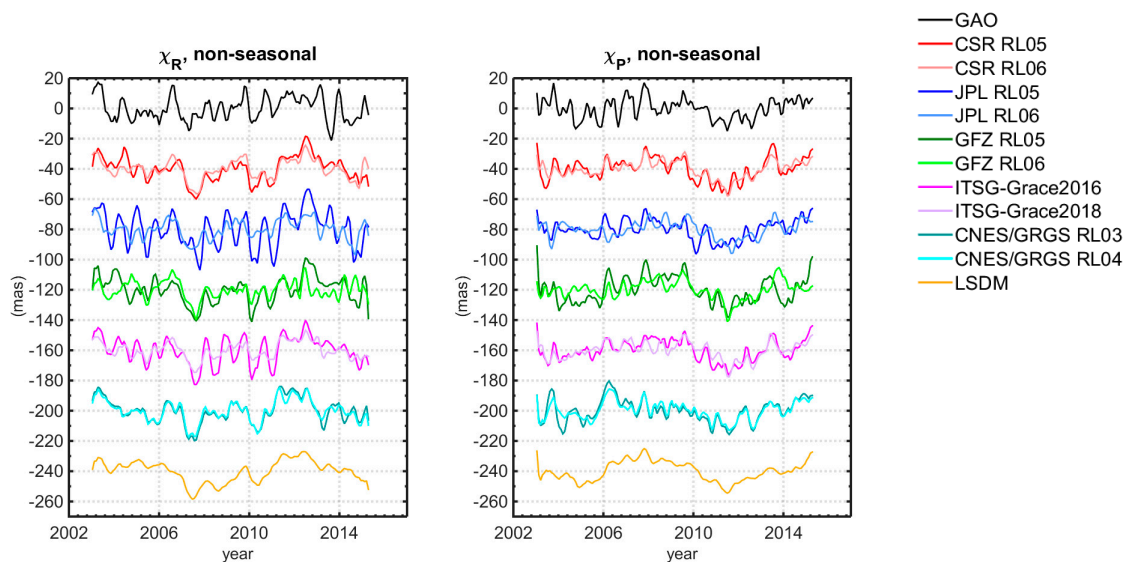


Figure 3. Retrograde and prograde parts (χ_R and χ_P , respectively) of non-seasonal variation in GAO, in HAM computed from different GRACE solutions, and HAM from the LSDM. The units are milliseconds of arc (mas). For better visibility, a bias was added to various HAM in order to shift them relative to each other.

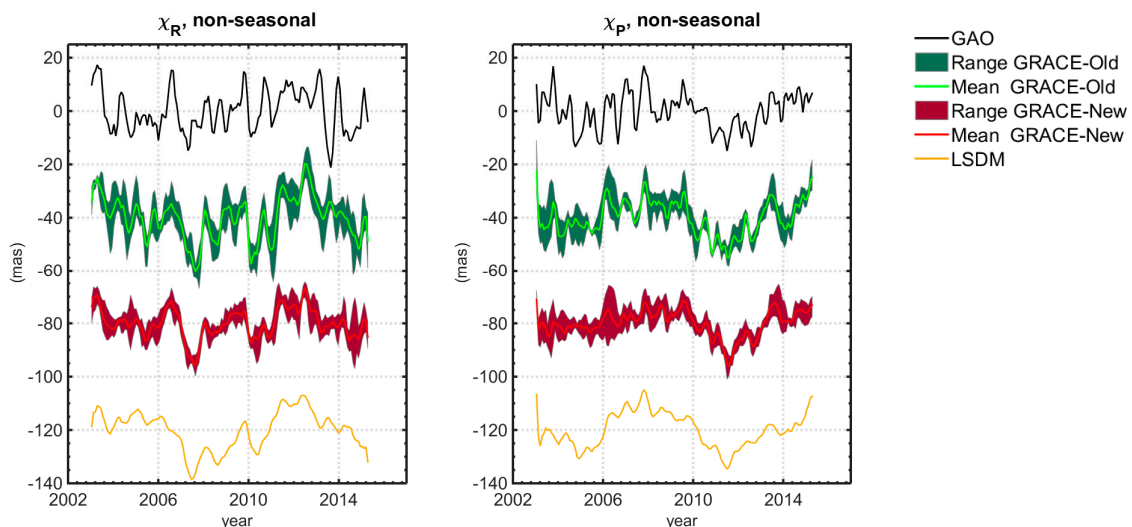


Figure 4. Comparison of mean value with ranges between minimum and maximum for χ_R and χ_P of non-seasonal variation in HAM for old and new GRACE solutions. Time series of GAO and HAM from the LSDM are provided for comparison. The units are milliseconds of arc (mas). For better visibility, a bias was added to various HAM in order to shift them relative to each other.

As shown in Figure 3, the non-seasonal oscillations in GAO and HAM were characterized by both long-term and short-term oscillations. The main contributors to long-term non-seasonal variations in HAM are groundwater changes [57] and mass loss of ice sheets and glaciers caused mainly by the

warming climate [57–59]. Other contributors include core-mantle coupling [60] and the flattening of the inner core and its tilt angle with respect to the outer core and mantle [61,62]. At shorter timescales (a few years or less), the main contributors to PM changes are atmosphere and land hydrosphere [4,63]. Keeping this in mind, we now decompose GAO and HAM series into long-term and short-term variations with periods of <730 days (Figures 5 and 6) and >730 days (Figures 7 and 8), respectively.

The comparison of Figures 1 and 2 with Figures 5 and 6 and values in Table A1 shows that the seasonal variations (Figures 1 and 2) appeared to have weaker amplitudes than non-seasonal short ones (Figures 5 and 6). However, previous research [4,63] emphasized that the land hydrosphere had the highest impact on PM excitation at seasonal time scales. Similar to the non-seasonal variations (Figures 3 and 4), for shorter non-seasonal periods obtained from old GRACE data, the χ_R produced higher amplitudes than χ_P , which was especially evident for JPL RL05 and ITSG-Grace2016. With the new GRACE solutions, these characteristics were less apparent. We observed a decrease in amplitudes and STD in the new HAM series and noted that this change was most evident for χ_R terms of JPL- and ITSG-based excitation functions. Most of the short-term non-seasonal variations computed from old GRACE solutions had amplitudes comparable or larger than the amplitude variability observed in GAO, especially in the χ_R part, whereas both the new solutions and the LSDM rather underestimated GAO amplitudes (Figures 5 and 6). The comparison of the mean χ_P and χ_R short-term non-seasonal changes with ranges between minimum and maximum (Figure 6) shows that results from the new GRACE solutions were more consistent in the χ_R part, but visible differences between particular solutions remained for the χ_P part, despite decreased amplitudes.

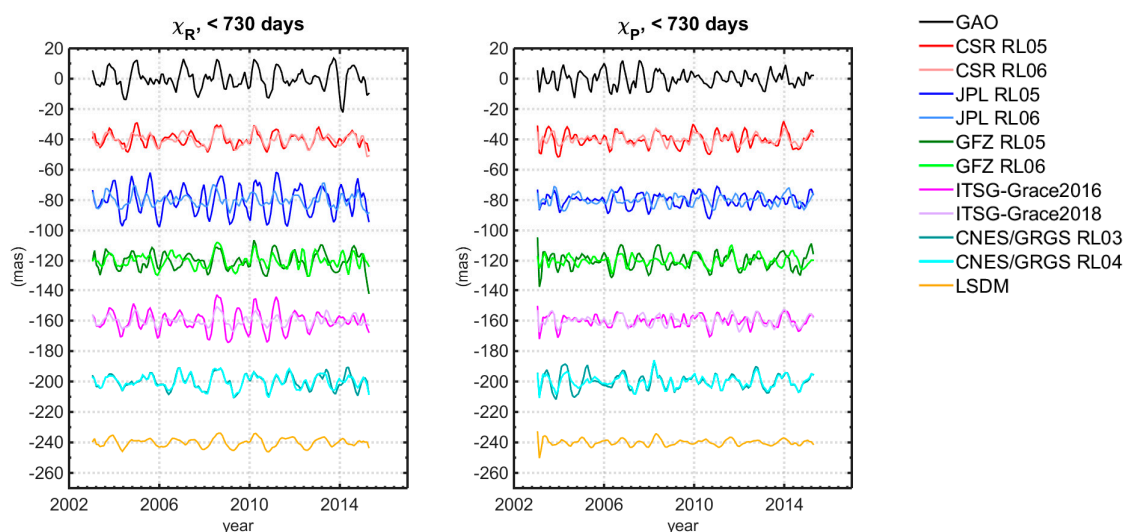


Figure 5. Retrograde and prograde parts (χ_R and χ_P , respectively) of short-term (<730 days) non-seasonal variation in GAO, in HAM computed from different GRACE solutions, and HAM from the LSDM. The units are milliseconds of arc (mas). For better visibility, a bias was added to various HAM in order to shift them relative to each other.

The χ_P and χ_R parts of long-term non-seasonal GAO and HAM are presented in Figures 7 and 8. In general, comparison of new GRACE data with old data revealed that the amplitudes of longer oscillations changed less than those for shorter periods. The magnitude of HAM was affected only slightly for the JPL and GFZ solutions. Notably, HAM series computed from the LSDM revealed an overestimation in the amplitudes of observed PM excitation, whereas they visibly underestimated them in the case of shorter variations (Figure 5). Regardless of whether old or new GRACE data were used, for the χ_R term, GRACE-based HAM series were characterized by higher STD and bigger amplitudes than GAO. For the χ_P part of the oscillations, the STDs of HAM were more consistent with the STDs of the reference series. The small amplitude change obtained after updating GRACE models from

RL05 to RL06 resulted in a small increase in consistency between different HAM estimations (Figure 8). Different GRACE solutions were revealed to be more consistent for the χ_R term than for the χ_P term.

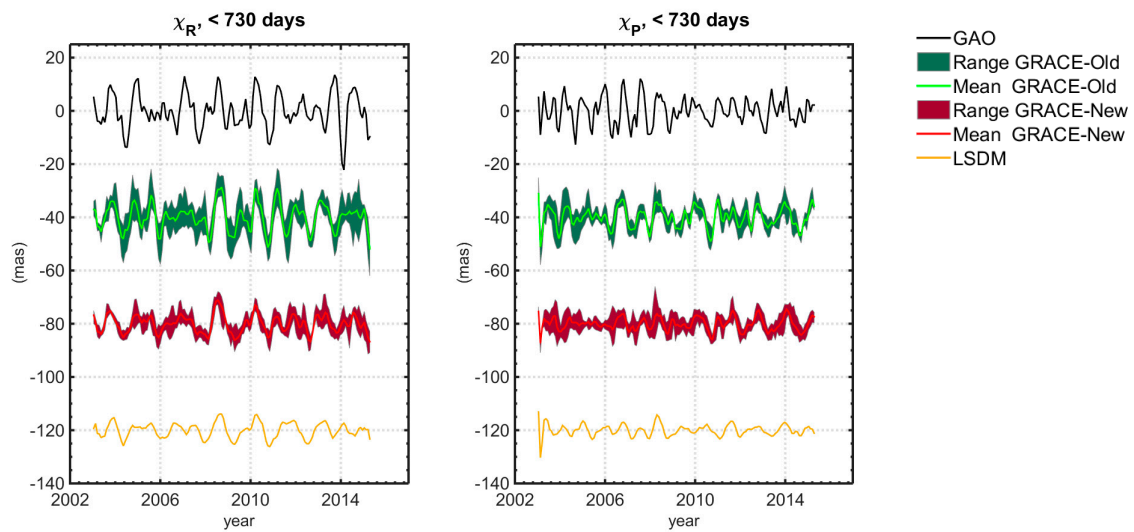


Figure 6. Comparison of mean value with ranges between minimum and maximum for χ_R and χ_P of short-term (<730 days) non-seasonal variation in HAM for old and new GRACE solutions. Time series of GAO and HAM from the LSDM are provided for comparison. The units are milliseconds of arc (mas). For better visibility, a bias was added to various HAM in order to shift them relative to each other.

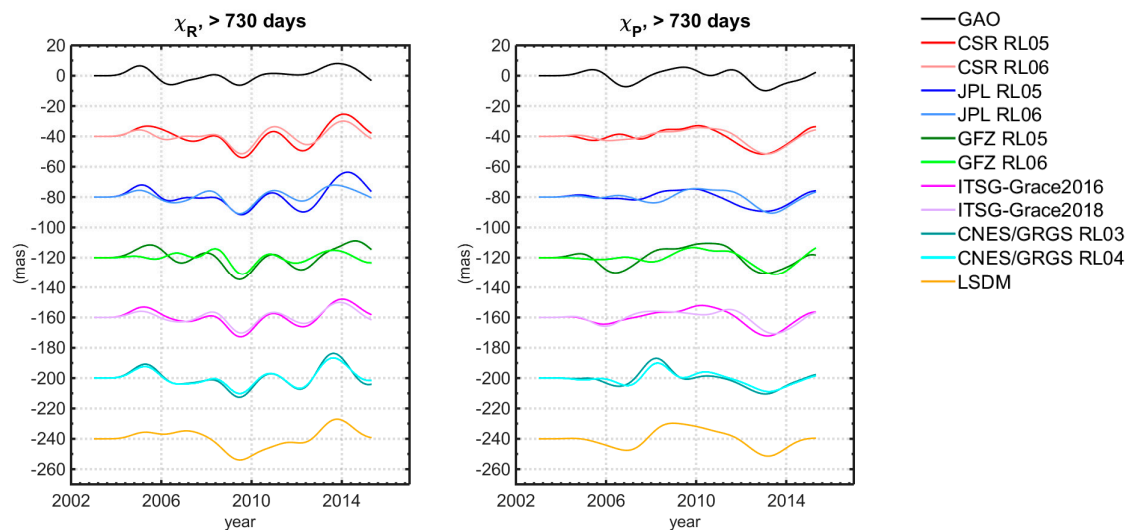


Figure 7. Retrograde and prograde parts (χ_R and χ_P , respectively) of long-term (>730 days) non-seasonal variation in GAO, in HAM computed from different GRACE solutions, and HAM from the LSDM. The units are milliseconds of arc (mas). For better visibility, a bias was added to various HAM in order to shift them relative to each other.

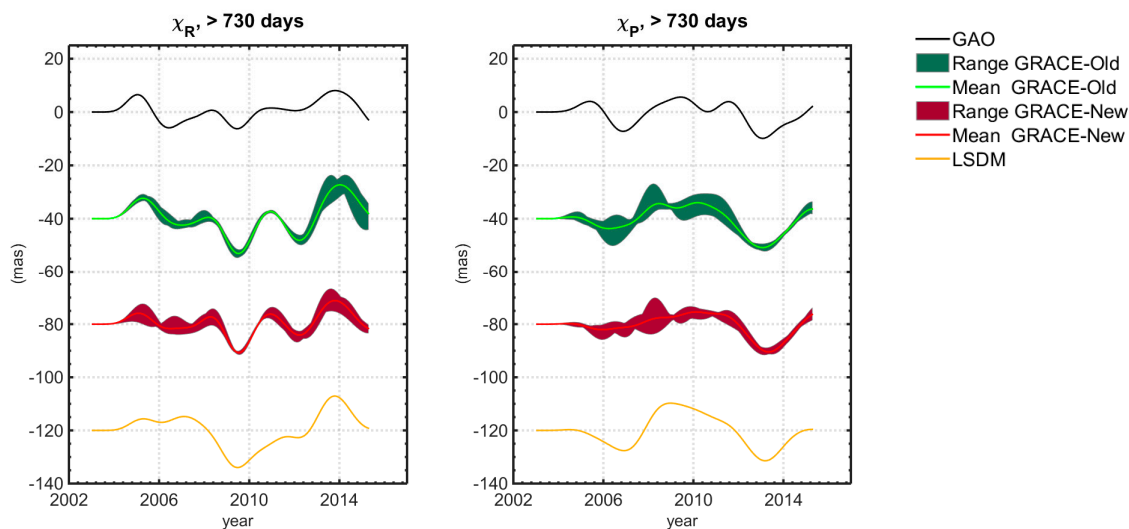


Figure 8. Comparison of mean value with ranges between minimum and maximum for χ_R and χ_P of long-term (>730 days) non-seasonal variation in HAM for old and new GRACE solutions. Time series of GAO and HAM from the LSDM are provided for comparison. For better visibility, a bias was added to various HAM in order to shift them relative to each other.

We now extend our assessment of variability of time series shown in Figures 1–8 by introducing a more detailed analysis of their STDs. The STD values for each oscillation are given in Table A1 in the Appendix A. To compare the STD of different HAM with STD of reference GAO series, we computed percent error in STD as follows:

$$\text{STD error} = [(\text{STD}_{\text{HAM}} - \text{STD}_{\text{GAO}}) / (\text{STD}_{\text{GAO}})] \cdot 100\%, \quad (6)$$

where positive results indicate higher STD for HAM series and negative results indicate higher STD for GAO (Table 1). For seasonal variations, almost all GRACE solutions underestimated the STD of HAM as each value of STD error is negative (except χ_R for JPL RL05), and a higher disagreement with GAO was observed for the χ_R term. This result corresponds with Figure 1, which reveals that seasonal amplitudes of χ_P for GAO were visibly stronger than for GRACE-derived HAM. Conversely, in the long-term non-seasonal spectral band, GRACE-based HAM series overestimated the STD of the reference data. For non-seasonal and non-seasonal short-term variations, the results are mixed and depend on the solution considered. In general, the highest STD agreement between HAM and GAO was obtained in the non-seasonal spectral band, whereas the lowest was found for seasonal oscillations. Taking into consideration absolute values of STD error, we can generally conclude that, with the new GRACE RL06 data, a percent error of STD has decreased for long-term non-seasonal changes, but increased for short-term oscillations.

Finally, to quantify the change of STD in HAM from new GRACE solutions compared with the old solutions, we computed the percentage of STD change as follows:

$$\text{STD change} = [(\text{STD}_{\text{new}} - \text{STD}_{\text{old}}) / (\text{STD}_{\text{old}})] \cdot 100\%, \quad (7)$$

where positive values indicate an increase of STD and negative values indicate a decrease of STD (Table 2). Besides seasonal changes for CSR, CNES/GRGS, and ITSG solutions, all HAM from new GRACE solutions had a decreased STD for all oscillations, and the highest change was observed for JPL and GFZ solutions. These results correspond with findings from our previous work [64], in which we compared equatorial components of HAM derived from different GRACE solutions. In that study, we noted that JPL data revealed the highest STD and amplitude change in RL06 compared with RL05 of all evaluated solutions for both seasonal and non-seasonal HAM variation.

Table 1. Percentage error of standard deviation (STD) of hydrological angular momentum (HAM) computed from Gravity Recovery and Climate Experiment (GRACE) solutions and HAM from the land surface discharge model (LSDM). ITSG, Institute of Theoretical Geodesy and Satellite Geodesy; GFZ, GeoForschungsZentrum; CSR, Centre for Space Research; JPL, Jet Propulsion Laboratory; CNES/GRGS, Centre National d’Etudes Spatiales/Groupe de Recherche de Géodésie Spatiale.

Series	Percentage Error of STD							
	Seasonal		Non-Seasonal		Non-Seasonal Short		Non-Seasonal Long	
	XR	XP	XR	XP	XR	XP	XR	XP
CSR RL05	−68	−29	2	8	−36	−5	77	19
CSR RL06	−63	−13	−20	−15	−41	−37	23	8
JPL RL05	−52	8	48	−5	37	−14	79	−1
JPL RL06	−69	−31	−21	−17	−39	−31	13	−2
GFZ RL05	−68	−36	8	28	−14	6	66	49
GFZ RL06	−77	−44	−26	−11	−32	−31	−6	7
CNES/GRGS RL03	−73	−49	1	13	−31	1	72	23
CNES/GRGS RL04	−72	−39	−11	−10	−35	−21	43	0
ITSG-Grace2016	−76	−55	13	2	0	−24	49	23
ITSG-Grace2018	−71	−28	−29	−14	−51	−32	14	5
LSDM	−34	−38	−10	−3	−58	−58	70	43

Table 2. The change of STD for HAM from new GRACE solutions compared with HAM from the older GRACE solutions.

Series	STD Change (%)							
	Seasonal		Non-Seasonal		Non-Seasonal Short		Non-Seasonal Long	
	XR	XP	XR	XP	XR	XP	XR	XP
CSR	16	23	−22	−21	−8	−33	−3	−9
JPL	−37	−36	−46	−12	−55	−20	−37	−1
GFZ	−29	−13	−31	−31	−21	−35	−44	−28
CNES/GRGS	5	19	−12	−20	−6	−22	−17	−19
ITSG-Grace	19	62	−37	−16	−51	−10	−23	−15

4.2. Agreement between HAM and GAO

We now analyse the agreement between different HAM series and GAO by computing correlation coefficients, relative explained variance, and standard deviation of differences between HAM and GAO, for each oscillation separately (Figures 9–12 and Tables A2–A5 in the Appendix A). The correlation plots were supplemented with information about the critical value of the correlation coefficient and the standard error of the difference between two correlation coefficients. The critical value of the correlation coefficient can be determined based on interpretation of autocorrelation function and statistical tables for Student’s *t*-test [8]. The autocorrelation function of the time series shows how rapidly the series changes and does not consider its previous values [65,66]. It shows the length of the time lag after which an evaluated series becomes decorrelated, meaning that the correlation between one series and the same series shifted with a lag is zero. Usually, the decorrelation time is assumed using one of the following four methods: (1) it is assumed to be the time required for autocorrelation function drop to the first zero crossing, (2) it is assumed to be the time required for autocorrelation function drop to $1/e$, (3) it is assumed to be double the time required for autocorrelation function drop to $1/2$, or (4) it is assumed to be double the time required for autocorrelation function drop to $1/e$ [66]. In this paper, we first determined decorrelation time using method (2) and then computed a number of independent points by dividing the number of series points by the decorrelation time. Finally, the critical value of correlation coefficient for computed number of independent points and assumed significance level (here we assumed 95%) was read from the Student’s *t*-test statistical tables. The standard error of a difference between two correlation coefficients was computed as $\sqrt{2/(N-3)}$, where N is a number of independent points.

Relative explained variance (Var_{exp}) is commonly used for estimating the discrepancy between a model (evaluated series, here HAM) and actual data (reference series, here GAO). It is the part of the total variance of reference data that is explained by evaluated data. The percentage of GAO variance explained by HAM was computed here as follows:

$$\text{Var}_{\text{exp}} = \left(\frac{\text{Var}^{\text{GAO}} - \text{Var}^{(\text{GAO}-\text{HAM})}}{\text{Var}^{(\text{GAO})}} \right) \cdot 100\%, \quad (8)$$

where $\text{Var}^{(\text{GAO})}$, $\text{Var}^{(\text{HAM})}$, and $\text{Var}^{(\text{GAO}-\text{HAM})}$ are variance of GAO (reference series), variance of HAM (evaluated series), and variance of a difference between GAO and HAM, respectively. The higher the value of Var_{exp} , the stronger the association between the evaluated and reference series. The optimal Var_{exp} value is 100%, which means in our case that HAM explains the full variance of GAO. For this case, the differences between reference and evaluated series are the same for all points of the time series. In other words, the variance of these differences is equal to zero. As the variance of differences $\text{Var}^{(\text{GAO}-\text{HAM})}$ between GAO or HAM increases, the Var_{exp} decreases. A similar method of quality assessment of the time series is to compute standard deviation of differences (STD_{diff}) between reference and evaluated data. The lower the STD_{diff} values, the better the evaluated series (optimal value of STD_{diff} is 0). However, because the computation of both Var_{exp} and STD_{diff} is based on STD or variance of differences between GAO and HAM, these parameters show the same characteristics of assessed data, and can lead to the similar conclusions. Therefore, we focused here only on detailed Var_{exp} analysis. The values of STD_{diff} are given in Tables A2–A5 (Appendix A)

We also look closer into the magnitude of improvement in correlation and variance agreement between GRACE-based HAM and GAO after releasing new GRACE solutions. To quantify the level of increase or decrease of these parameters in each new solution, we computed the percentage change of these parameters (Corr change and Var_{exp} change). Using these parameters, we examined how much correlation coefficients and Var_{exp} for RL06 were improved compared with correlation coefficients and Var_{exp} for RL05. The computations were performed for each pair of GRACE new and old solutions: CSR RL06 versus CSR RL05, JPL RL05 versus JPL RL06, GFZ RL06 versus GFZ RL05, CNES/GRGS RL04 versus CNES/GRGS RL03, and ITSG-Grace2018 versus ITSG-Grace2016. We used the following equations (Tables 3 and 4):

$$\text{Corr change} = [(\text{Corr}_{\text{new}} - \text{Corr}_{\text{old}}) / \text{abs}(\text{Corr}_{\text{mean old}})] \cdot 100\%, \quad (9)$$

$$\text{Var}_{\text{exp}} \text{ change} = [(\text{Var}_{\text{exp new}} - \text{Var}_{\text{exp old}}) / \text{abs}(\text{Var}_{\text{exp mean old}})] \cdot 100\%, \quad (10)$$

where abs means absolute values, $\text{Corr}_{\text{mean old}}$ is a mean correlation coefficient for all old GRACE solutions, $\text{Var}_{\text{exp mean old}}$ is a mean relative explained variance for all old GRACE solutions, positive results indicate improvement, and negative results indicate deterioration. Tables 5 and 6 were supplemented with values for the mean GRACE correlations and variances.

Figure 9 shows that, in the seasonal part of the spectrum, the CSR RL06 solution provided the highest correlation of HAM with GAO (0.87) for the χ_R term, whereas the best result for the χ_P part was obtained for CNES/GRGS RL03 and CNES/GRGS RL04 (0.74 and 0.73, respectively). For both χ_R and χ_P terms, HAM from JPL solutions (both RL05 and RL06) provided the worst agreement with reference data, with correlations far below the required level for statistical significance. Very low correlation coefficients for JPL data were a result of phase differences between the two sinusoids representing seasonal variations for GAO and JPL-based HAM. We found an increase of correlation coefficients with GAO for HAM from new GRACE data compared with the older ones (except ITSG for the χ_R term and JPL for the χ_P term). For the χ_R term, the biggest correlation improvement was detected for the JPL solution, whereas for the χ_P term, correlation improvement was highest for ITSG (Table 3). Similar to the correlation results, the highest relative explained variance was obtained for CSR RL06 in χ_R (51%) and for CNES/GRGS RL03 and CNES/GRGS RL04 in χ_P (49% and 52%, respectively). The highest

variance improvement was detected for the JPL solution in the χ_R part and for the ITSG solution in χ_P part of the seasonal variation (Table 4). It should be noted that the HAM function obtained from LSDM revealed a very good agreement with reference GAO series, but only in the χ_R part (correlation coefficient of 0.74 and relative explained variance of 54%).

Table 3. Improvement in correlation between HAM and GAO for new GRACE solutions compared with the older solutions (positive, increased correlation; negative, decreased correlation).

Series	Correlation Improvement (%)							
	Seasonal		Non-Seasonal		Non-Seasonal Short		Non-Seasonal Long	
	χ_R	χ_P	χ_R	χ_P	χ_R	χ_P	χ_R	χ_P
CSR	8	30	34	30	47	38	10	23
JPL	186	-52	11	-37	-18	-103	21	-3
GFZ	54	41	-26	-33	-15	-99	-19	-11
CNES/GRGS	-9	-2	-1	6	-2	-6	2	17
ITSG-Grace	-34	83	30	3	49	9	9	-8
Mean	23	20	10	-6	12	-32	5	3

Table 4. The improvement in relative explained variance between HAM and GAO for new GRACE solutions compared with the older solutions (positive, increased relative explained variance; negative, decreased relative explained variance).

Series	Relative Explained Variance Improvement (%)							
	Seasonal		Non-Seasonal		Non-Seasonal Short		Non-Seasonal Long	
	χ_R	χ_P	χ_R	χ_P	χ_R	χ_P	χ_R	χ_P
CSR	65	198	165	1127	86	1637	272	211
JPL	563	200	384	-621	366	-1681	349	-16
GFZ	5	345	56	-8	32	-1495	182	102
CNES/GRGS	-6	37	37	646	9	586	123	221
ITSG-Grace	-21	539	207	328	216	332	134	16
Mean	121	264	170	294	142	-124	212	107

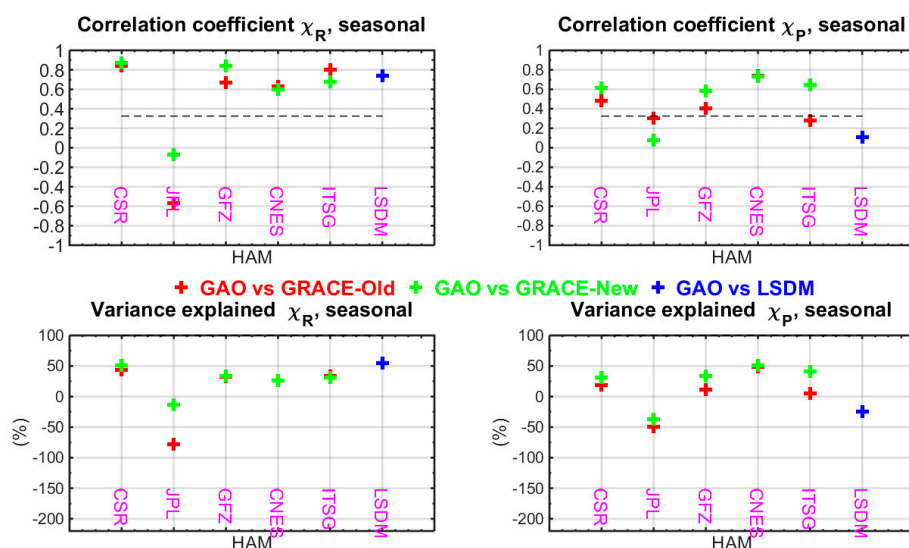


Figure 9. Correlation coefficients of χ_R and χ_P parts of seasonal variation between GAO and HAM computed from GRACE solutions and the LSDM and percentage of variance in GAO explained by HAM functions. The critical value of the correlation coefficient for 25 independent points and a confidence level of 0.95 was 0.34. The standard error of the difference between two correlation coefficients for 25 independent points was 0.30.

In the non-seasonal spectral band, for χ_R , the correlation and variance agreement improved notably in all new solutions except for GFZ; however, for χ_P , a visible correlation increase was observed only in CSR (Figure 10, Table 3). The best correlation agreement with GAO for both χ_P and χ_R terms was detected for CSR RL06 (0.66 and 0.68 for χ_R and χ_P , respectively) and ITSG-Grace2018 (0.64 and 0.59 for χ_R and χ_P , respectively). The comparison of relative explained variances provided similar conclusions, with the best results for CSR RL06 (42% and 44% for χ_R and χ_P , respectively) and ITSG-Grace2018 (40% and 28% for χ_R and χ_P , respectively). However, despite some improvement in the results using the new GRACE RL06 data, the variance agreement was still unsatisfactory as none of the values exceeded 45% and many negative variances occurred. In the χ_P part of the hydrological excitation, LSDM-based HAM provided results comparable with those obtained for CSR RL06 and ITSG-Grace2018 (correlation coefficient of 0.64 and relative explained variance of 29%).

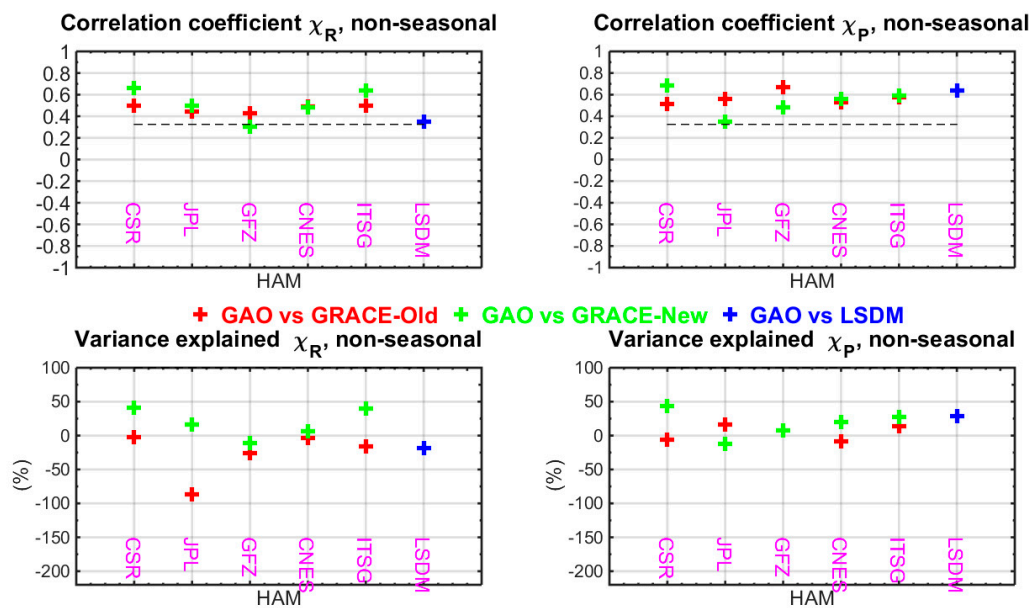


Figure 10. Correlation coefficients of χ_R and χ_P parts of non-seasonal variation between GAO and HAM computed from GRACE solutions and the LSDM and the percentage of variance in GAO explained by HAM functions. The critical value of the correlation coefficient for 25 independent points and a confidence level of 0.95 was 0.34. The standard error of the difference between two correlation coefficients for 25 independent points was 0.30.

For short-term non-seasonal variation in HAM, only CSR RL06 and ITSG-Grace2018 provided correlation coefficients visibly above the statistical significance level for both χ_R and χ_P circular terms (Figure 11). These GRACE models are the only ones to show a visible improvement in HAM correlation with GAO compared with the previous releases (Table 3). Notably, HAM from the GFZ RL05 solution was characterized by the best correlation agreement in the χ_P part of the hydrological excitation (0.65); however, in the χ_R part, this consistency was poor. HAM computed using the new GFZ and JPL solutions was revealed to decrease correlation with GAO compared with the older GRACE data, and this was visible especially in χ_P (Table 3). Similar findings were shown from an analysis of relative explained variances—in χ_R , the best results were provided by CSR RL06 and ITSG-Grace2018 (40% and 31%, respectively), whereas in χ_P , the highest variances were obtained for HAM derived from GFZ RL05, CSR RL06, and ITSG-Grace2018 (25%, 29%, and 20%, respectively). Apart from χ_P for JPL and GFZ data, all new solutions revealed an improvement in variance agreement with GAO compared with the old solutions.

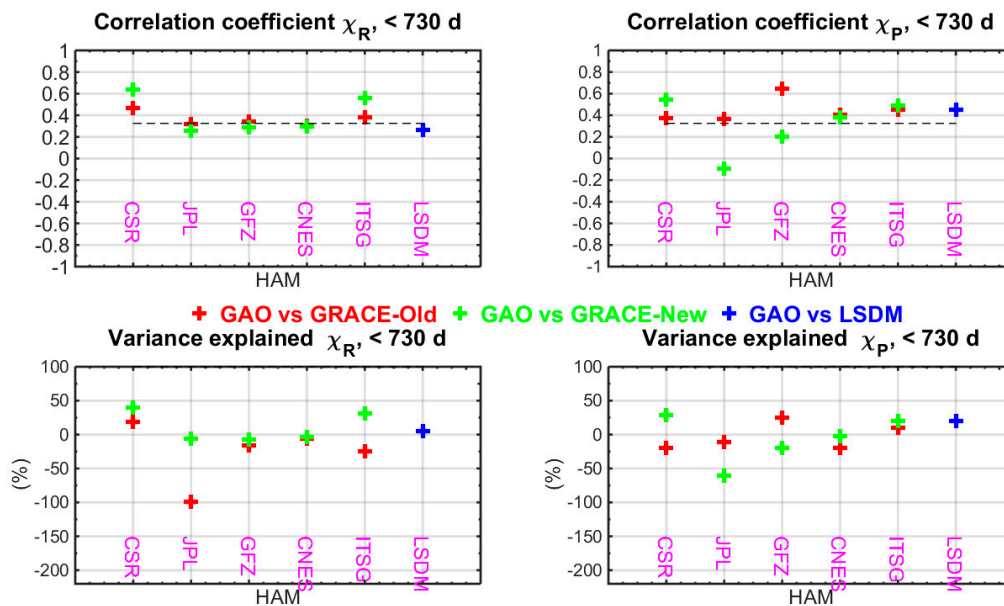


Figure 11. Correlation coefficients of χ_R and χ_P parts of short-term (<730 days) non-seasonal variation between GAO and HAM computed from GRACE solutions and the LSDM and the percentage of variance in GAO explained by HAM functions. The critical value of the correlation coefficient for 25 independent points and a confidence level of 0.95 was 0.34. The standard error of the difference between two correlation coefficients for 25 independent points was 0.30.

The data presented in Figure 12 suggest that long-term changes in the hydrological part of PM excitation are much better determined by GRACE observations than the shorter period variations. This is unsurprising as short oscillations are more diverse than long ones, which could affect the magnitude of correlation coefficients between HAM and GAO. Moreover, the fact that GRACE solutions are provided in only monthly intervals with occasional gaps in data might also have contributed. Similar conclusions were drawn from our previous work [10], where we focused on analysis of the equatorial components (χ_1 , χ_2) of PM excitation. As shown in Figure 12, for the χ_R part, almost all new solutions provided correlation agreement between HAM and GAO at the level of 0.80 or more (except GFZ RL06), with the best results for JPL RL06, CNES/GRGS RL04, and ITSG-Grace2018 (correlation coefficients equal to 0.87, 0.86, and 0.85, respectively). Similarly, for χ_P , correlation coefficients exceeded 0.70 for all HAM functions and the highest value was obtained for CSR RL06 (0.81). However, a notable correlation improvement in new GRACE data was detected only for CSR and JPL solutions in χ_R , and for CSR and CNES/GRGS in χ_P (Table 3). In terms of relative explained variance, the most satisfactory results were for JPL RL06 (69%) and ITSG-Grace2018 (64%) for χ_R , and CSR RL06 for χ_P (57%). Notably, for the χ_R part of excitation, we observed visible variance improvement in HAM functions obtained from the GRACE RL06 solutions compared with the RL05 solutions (Table 4). Similar to the seasonal χ_R and non-seasonal χ_P terms, long-term χ_P oscillations were very well modelled by the LSDM.

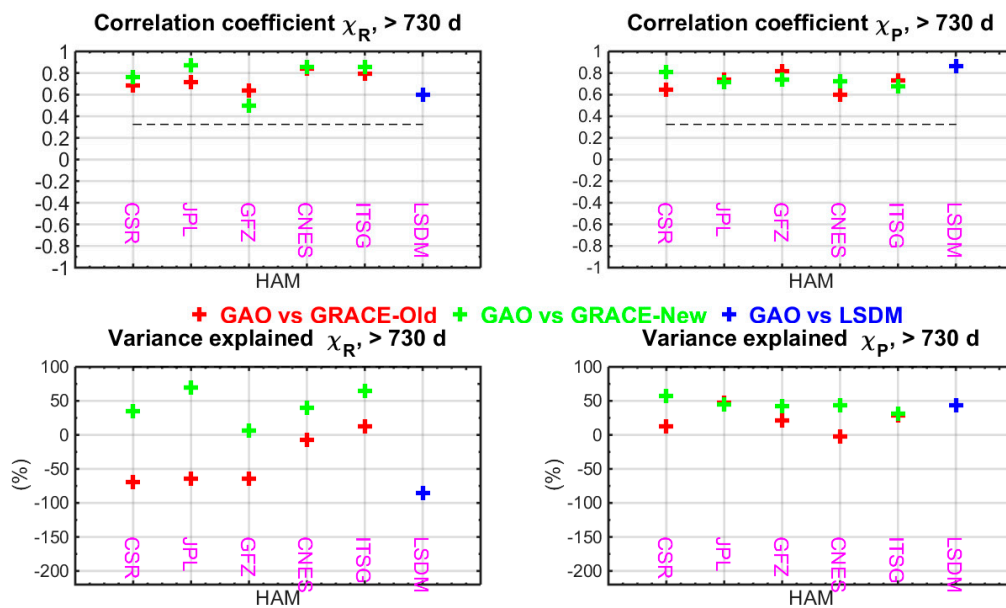


Figure 12. Correlation coefficients of χ_R and χ_P parts of long-term (>730 days) non-seasonal variation between GAO and HAM computed from GRACE solutions and the LSDM and the percentage of variance in GAO explained by HAM functions. The critical value of the correlation coefficient for 25 independent points and a confidence level of 0.95 was 0.34. The standard error of the difference between two correlation coefficients for 25 independent points was 0.30.

The more detailed analysis of values given in Table 3 allows us to conclude that CSR is the only solution for which there was correlation improvement between HAM and GAO in RL06 compared with RL05 for both χ_P and χ_R and for all oscillations. The biggest correlation improvement was detected for the JPL solution in the χ_R seasonal term (186% improvement) and for the ITSG solution in the χ_P seasonal term (83% improvement). Our previous work, which evaluated χ_1 and χ_2 [64], also showed that, for the seasonal part of HAM, the JPL solution was distinguished by the greater improvement in consistency with GAO than other solutions. This was mainly because new the JPL data were smoother than the older data. Notably, we also observed a decrease in correlation, which mostly affected the GFZ and JPL solutions and was highest for the χ_P part of the non-seasonal short-term variations (maximum decrease for JPL—103% and for GFZ—99%). With the release of new GRACE solutions, HAM from the CNES/GRGS series produced the lowest correlation change, which did not exceed $\pm 9\%$ (except for the χ_P term in the non-seasonal long-term variation). Taking into account the mean correlation change, the seasonal correlations showed the greatest improvement (23% improvement for χ_R and 20% improvement for χ_P), whereas the smallest change was observed for the long-term non-seasonal spectral band. We noted a correlation decrease for the χ_P part of the non-seasonal short-term variation (32% decrease) and for the χ_P part of non-seasonal variation (6% decrease).

Table 4 shows that only HAM derived from the CSR solution improved variance agreement with GAO for both χ_P and χ_R and for all oscillations. However, in contrast to the correlation changes, there were fewer cases in which there was a notable decrease in variance agreement between HAM and GAO (only for χ_P in non-seasonal short-term variation for JPL and GFZ, and for χ_P in non-seasonal variation for JPL). The highest variance improvement for both χ_P and χ_R was observed for CSR in the non-seasonal spectral band and for JPL in seasonal spectral band. Taking into consideration the mean variance change, apart from the χ_P term of short-period changes, we detected a notable variance improvement for all oscillations, which exceeded 100%. These findings reveal that the mean variance improvement was several times greater than the mean correlation improvement.

At this point, it should be mentioned that our validation of χ_P and χ_R terms in GRACE-based HAM was based on correlation coefficients with GAO and relative explained variances, but there are other metrics that can be helpful in such an evaluation. The use of coefficient of determination (R^2)

values from a linear regression analysis is a common method for such interpretation of the results. The R^2 value shows quality of the model's fit to the data and ranges between 0 and 1 (with 1 being the best value). R^2 is often used in validation of hydrological models [67], but it can be also used in assessment of other data types. Therefore, we computed R^2 between GAO and different HAM and showed the results in Figure 13 (for seasonal and non-seasonal changes) and Figure 14 (for non-seasonal short-term and non-seasonal long-term changes). However, the analysis of R^2 led us to the similar conclusions as a comparison of correlation coefficients. In particular, for seasonal variations, the highest R^2 values were obtained for CSR RL06 (for χ_R), GFZ RL06 (for χ_R), and CNES/GRGS RL04 (for χ_P); for non-seasonal and non-seasonal short-term variations, the highest R^2 values were observed for CSR RL06 (for χ_R and χ_P), ITSG-Grace2018 (for χ_R), and GFZ RL05 (for χ_P); for non-seasonal long-term changes, the highest R^2 values were obtained for JPL RL06 (for χ_R), CNES/GRGS RL03 and RL04 (for χ_R), ITSG-Grace2018 (for χ_R), CSR RL06 (for χ_P), GFZ RL05 (for χ_P), and LSDM (for χ_P).

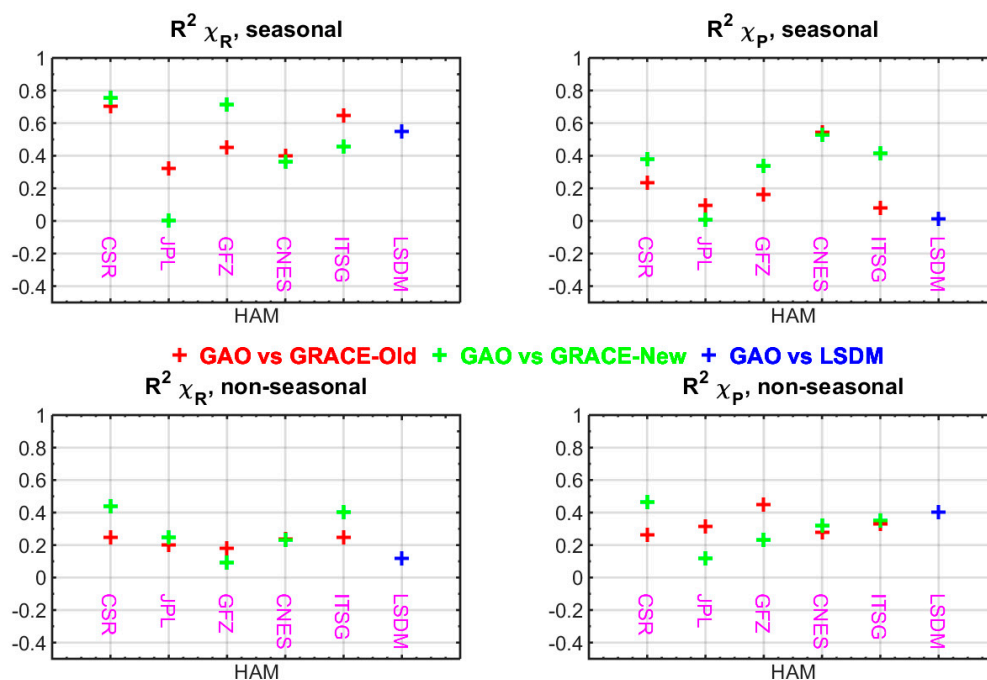


Figure 13. Coefficients of determination (R^2) for χ_R and χ_P parts of seasonal (top panel) and non-seasonal variation between GAO and HAM computed from GRACE solutions and the LSDM.

In contrast to the previous studies, which demonstrated good results for χ_2 and clearly worse results for χ_1 [3,7,9–14,23,27,63,68], it was difficult to conclude whether the χ_P term or the χ_R term is better modelled by GRACE as results depended on the solution and oscillation considered. Moreover, in terms of correlation and variance agreement with GAO, there was no noticeable difference between χ_P and χ_R . To make the results more general and readable, we next computed the mean correlation and variance from all old GRACE solutions, and then the mean correlation and variance from all new GRACE solutions, for different variations separately (Tables 5 and 6). The tables are supplemented with corresponding values for HAM from LSDM. In terms of the correlations, the differences in results between the χ_P and χ_R terms was small and did not exceed 0.1, and for new GRACE RL06 solutions, they were even smaller (Table 5). Similarly, the variance explained values obtained for these new GRACE data reveal that HAM agreed better in the χ_R than in the χ_P term only for non-seasonal short-term variations (11% and -7% , respectively) (Table 6). For other oscillations in HAM determined from GRACE RL06 data, the variance results were almost identical for both terms as the variance differences between χ_P and χ_R did not exceed one percentage point. For GRACE RL05 solutions, these discrepancies were slightly higher, but it remains unclear which term is better modelled by GRACE RL05 data. For HAM obtained from the LSDM, the discrepancies in results between χ_P and χ_R were

more evident—both correlation coefficients and relative explained variances were higher for the χ_R term in the seasonal spectral band, whereas for all non-seasonal variations, these parameters were higher for the χ_P term. For LSDM, the maximum correlation difference between χ_P and χ_R reached 0.63 (for seasonal changes), whereas the maximum variance difference was equal to 129 percentage points (for non-seasonal long-term changes).

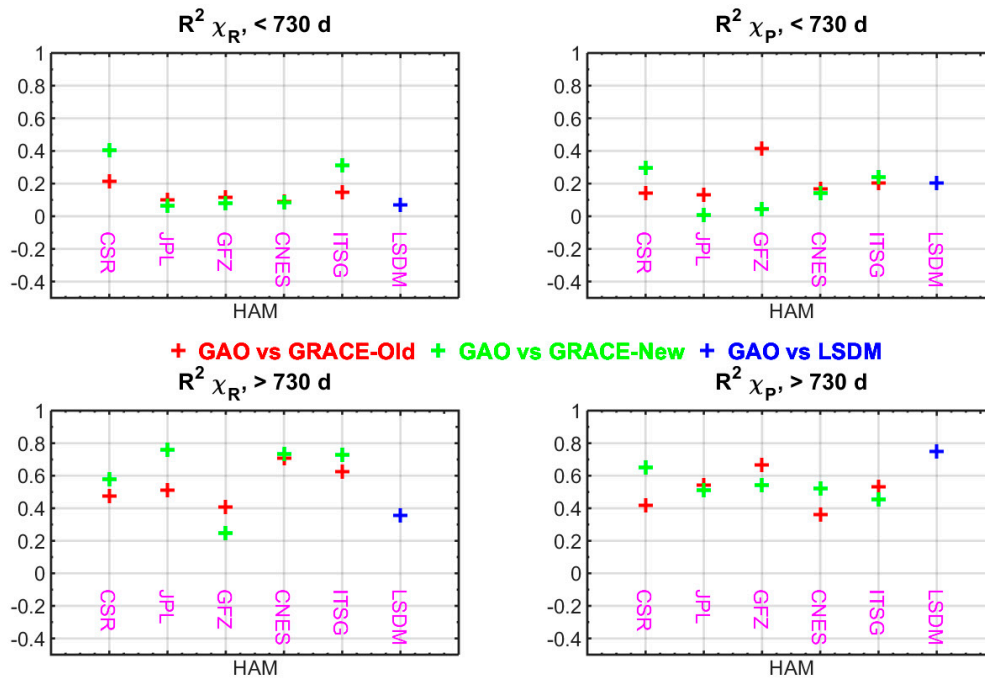


Figure 14. Coefficients of determination (R^2) for χ_R and χ_P parts of short-term (<730 days) non-seasonal (top panel) and long-term (>730 days) non-seasonal (bottom panel) variation between GAO and HAM computed from GRACE solutions and the LSDM.

Tables 5 and 6 also indicate that, in general, the highest improvement in correlation with the new GRACE RL06 data was obtained for seasonal variation. However, in the short-term spectral band, the correlation with GAO dropped for the χ_P term, which contributed to a slight correlation decrease in this term for non-separated non-seasonal change (short-term plus long-term). In terms of relative explained variances, the agreement with GAO was improved in almost all considered spectral bands (except χ_P in non-seasonal short-term variations), which might be a result of amplitude changes in HAM computed from the new GRACE data. Nevertheless, it should be kept in mind that such conclusions are general and are based on the mean of GRACE solutions. The results for various solutions differed from each other (see Figures 9–12).

Table 5. Mean values of correlation coefficients between GAO and GRACE-based HAM for each oscillation considered: mean GRACE old (the mean of correlations for CSR RL05, JPL RL05, GFZ RL05, CNES/GRGS RL03, and ITSG-Grace2016) and mean GRACE new (the mean of correlations for CSR RL06, JPL RL06, GFZ RL06, CNES/GRGS RL04, and ITSG-Grace2018). Correlation coefficients for HAM from the LSDM were added for comparison.

Series	Mean Correlation Coefficients							
	Seasonal		Non-Seasonal		Non-Seasonal Short		Non-Seasonal Long	
	χ_R	χ_P	χ_R	χ_P	χ_R	χ_P	χ_R	χ_P
Mean GRACE old	0.47	0.44	0.47	0.57	0.36	0.45	0.73	0.71
Mean GRACE new	0.58	0.53	0.52	0.53	0.41	0.30	0.77	0.73
LSDM	0.74	0.11	0.35	0.64	0.26	0.45	0.60	0.86

Table 6. Mean values of percentage variances in GAO explained by GRACE-based HAM for each oscillation considered: mean GRACE old (the mean of variances for CSR RL05, JPL RL05, GFZ RL05, CNES/GRGS RL03, and ITSG-Grace2016) and mean GRACE new (the mean of variances for CSR RL06, JPL RL06, GFZ RL06, CNES/GRGS RL04, and ITSG-Grace2018). Relative explained variance for HAM from the LSDM were added for comparison.

Series	Mean Relative Explained Variance (%)							
	Seasonal		Non-Seasonal		Non-Seasonal Short		Non-Seasonal Long	
	XR	XP	XR	XP	XR	XP	XR	XP
mean GRACE old	12	7	−27	4	−25	−3	−38	21
mean GRACE new	25	24	19	18	11	−7	43	44
LSDM	54	−25	−19	29	5	20	−86	43

5. Discussion

In this section, we would like to address a few issues that should be discussed during the comparison between GAO and HAM and between different HAM. First of all, our results showed that both prograde and retrograde terms of polar motion excitation can be determined by GRACE with similar accuracy. However, it is well known [3,7,9–14,23,27,63,67] that, when equatorial components of HAM are considered, HAM is in better consistency with GAO for χ_1 than for χ_2 . The main reason for that is the spatial distribution of the main continents and oceans. The χ_1 component, which is directed towards the Greenwich Meridian, is closely related to the impact of ocean and Greenland ice mass changes, whereas the χ_2 component, directed towards 90 °E, is more sensitive to the mass redistribution on continents of the Northern Hemisphere. Therefore, it is not surprising that the χ_2 component of the hydrological excitation function, which is more sensitive to mass changes over land, is better correlated with GAO than χ_1 .

The paper compared HAM from the newest RL06 GRACE solution with previous RL05. It should be kept in mind that RL05 series are no longer recommended for use. There are many updates in RL06 data, but there are also differences among new solution from various data centres. The newly available RL06 from GRACE has benefited from a thorough reprocessing of the Level 1 sensor data, in particular the K-band range-rate observations and the star tracker data. Improvements were also realized from using a re-processed GPS (Global Positioning System) constellation, from refined data screening procedures that lead to a reduced number of apparently detected outliers, and from the revision of various parametrization schemes of both the K-band ranging and the accelerometers [43,45,47]. In addition, various background models were updated for RL06 including the new GRACE Atmosphere and Ocean De-Aliasing Level 1B [39,40] product, a new mean pole model [69], improved static gravity field and ocean tides models, and updated planetary ephemerides for perturbations induced by the large planets of the solar system [43,45,47]. The summary information on background models used for processing GRACE solutions that were considered here, together with data sources and references, is given in Table A6 in the Appendix A.

Regarding changes in how the mean pole tide is considered, while all new GRACE solutions used linear mean pole tide, in previous RL05 data, the cubic model was applied. Wahr et al. [70] suggested that RL05 solutions should be corrected by applying a pole tide correction to remove a non-hydrological signal from GRACE Level 2 solutions. This correction would make RL05 data more compatible with RL06. However, there are other drawbacks of RL05 data that have already been mentioned, which is why scientific institutes decided to improve processing methods and to release RL06. We should highlight that our intention was not to improve RL05 by including many corrections, but to compare them with RL06 and to assess the level of improvement. We focused on checking how updating some models and data processing methods in RL06 influenced an agreement between HAM and GAO.

Another difference between RL05 and RL06 solutions is different AOD1B data product [39,40], which provides non-tidal short-term mass variations in the atmosphere and the oceans. There are many modifications of this data compared with the previous version (AOD1B RL05), such as increased

spatial and temporal resolution, change of ocean model from the Ocean Model for Circulation and Tides (OMCT; [71]) to the MPIOM [41], and improved long-term consistency [39,40]. However, despite many changes in the GRACE dealiasing product, the authors of [23] showed that the update of this model plays a minor role in HAM improvement. Updating dealiasing products from AOD1B RL05 to AOD1B RL06 certainly benefits HAM in the short-term spectral band. Therefore, GAO and HAM series, which were downsampled in this paper into monthly changes, should not be affected by different AOD1B products. It should be also noted that, in the series from CNES/GRGS (both RL03 and RL04), in contrast to other new GRACE solutions, the AOD1B RL06 model was not used. The CNES dealiasing product was developed based on the ERA-interim (ECMWF reanalysis from January 1989 onward) for the atmospheric part, and the TUGO (Toulouse unstructured grid ocean) barotropic model for the oceanic response to the ERA-interim pressure and wind forcing [49].

We should emphasize that it is difficult to determine which processing changes caused the biggest improvement in GRACE-based polar motion excitation. The discrepancies between RL05 and RL06, and between solutions from the same release, but processed by different institutes, resulted from not only background models, but also calculation algorithms, methods of GRACE orbits determination, software, and others. Moreover, not all data processing details are made available to the users by data centers.

Another issue is tidal effects resulting from gravitational impact of Moon, Sun, and planets, which have a main impact on precession and nutation. However, it was reported that they also disturb polar motion, because they induce deformations of solid Earth and Earth fluids, causing inertia tensor changes [72]. Tidal changes in polar motion mainly concern ocean tides, which excite polar motion in diurnal, subdiurnal, and long-term bands. These effects were removed from GRACE solutions using the models (see Table A6), but they were not removed from GAM. It was reported in [33] that high-frequency (sub-daily) tidal signals in polar motion reach about 1 mas. However, C04 EOP daily series, which were used for computation of GAM and GAO, did not include these signals, because they are provided on a daily time rate. Among long-term ocean tides, the most important and often considered by studies (e.g., [72,73]) is a fortnightly ocean tide with frequency of 27 cycles per year. In our paper, we considered monthly changes, so diurnal, subdiurnal, and fortnightly ocean tides should not affect our results.

6. Summary and Conclusions

In this paper, we showed an alternative method of presenting the hydrological polar motion excitation function. In contrast to previous works, where authors used two equatorial components of HAM directed towards Greenwich Meridian (χ_1) and 90°E meridian (χ_2), we decomposed χ_1 and χ_2 into prograde and retrograde circular terms (χ_P and χ_R), using the CFT method. We evaluated the χ_P and χ_R components of HAM obtained from the GRACE RL05 and RL06 series and from the LSDM hydrological model by comparing them with the hydrological signal in GAO, obtained from precise measurements of the pole coordinates. The validation of GRACE-based and LSDM-based HAM was conducted for four different oscillations: seasonal, non-seasonal, non-seasonal short, and non-seasonal long.

Despite different methods of representation, our general remarks are congruous with those obtained in similar works dedicated to χ_1 and χ_2 analyses [23–25]. With the new GRACE RL06 data, the consistency between different solutions was increased. HAM from the new RL06 GRACE data is smoother than HAM from RL05 as STD and amplitudes of oscillations have decreased. The new GRACE solutions provided better correlation and variance explained agreement with observed PM excitation than the previous series. However, despite the improved agreement with reference data, there is still no satisfactory variance compatibility. The level of agreement between HAM and GAO depended on the oscillation considered and was higher for long-term variations than for short-term ones. For most of the oscillations considered, the highest agreement with reference data was obtained for the CSR RL06 and ITSG-Grace2018 solutions.

In new GRACE HAM functions, the correlation coefficients with GAO were improved by about 22–23% for seasonal and 3–5% for non-seasonal long-term variations. However, although correlation

in χ_R increased for non-seasonal and non-seasonal short changes by 10–12%, χ_P results worsened. In terms of average relative explained variance, apart from χ_P term in the non-seasonal short-term spectral band, the mean value of this parameter increased in HAM from new GRACE solutions by more than 100%. The average correlation coefficients between GAO and HAM from new GRACE data were at the level of 0.53–0.58 for seasonal, 0.52–0.53 for non-seasonal, 0.30–0.41 for non-seasonal short, and 0.73–0.77 for non-seasonal long variations. Accordingly, the relative explained variances were 24–25% for seasonal, 18–19% for non-seasonal, –7–11% for non-seasonal short, and 43–44% for non-seasonal long changes.

In contrast to χ_1 and χ_2 representation, where we observed significantly better results for the χ_2 than for the χ_1 component [23–25], the agreement with GAO was at a similar level for both χ_R and χ_P . The consistency in results between χ_R and χ_P terms increased with the new GRACE solutions. The exception to this feature was the HAM function obtained from the LSDM model processed by the GFZ, for which seasonal changes were better determined in χ_R , whereas non-seasonal changes were better determined in χ_P . The LSDM-based HAM revealed a notable correlation with GAO for non-seasonal χ_P and seasonal χ_R terms. We showed that χ_P and χ_R terms can be used in evaluation of hydrological excitation functions and the method of describing HAM (classical equatorial components or circular terms) does not affect the results. Our findings from GRACE data validation provided information on which GRACE solutions are the most suitable for PM investigations in specific spectral bands.

Author Contributions: Conceptualization, J.N. and J.Ś.; Data curation, J.N. and J.Ś.; Formal analysis, J.Ś.; Funding acquisition, J.N. and J.Ś.; Investigation, J.N. and J.Ś.; Methodology, J.N. and J.Ś.; Project administration, J.N.; Resources, J.N. and J.Ś.; Software, J.N.; Supervision, J.N.; Validation, J.Ś.; Visualization, J.N.; Writing—original draft, J.Ś.; Writing—review & editing, J.N. and J.Ś. All authors have read and agreed to the published version of the manuscript.

Funding: This research was funded by National Science Centre, Poland (NCN), grant number 2018/31/N/ST10/00209, and by the Polish National Agency for Academic Exchange (NAWA) grant number PPI/APM/2018/1/00032/U/001.

Acknowledgments: We would like to thank Waldemar Popiński for providing software for calculating prograde and retrograde terms using CFT. We would also like to thank two anonymous reviewers for their valuable comments that contributed to the improvement of the article.

Conflicts of Interest: The authors declare no conflict of interest.

List of Acronyms

AAM	atmospheric angular momentum
AOD1B	GRACE Atmosphere and Ocean De-Aliasing Level 1B
CFT	complex Fourier transform
CNES/GRGS	Centre National d'Etudes Spatiales/Groupe de Recherche de Géodésie Spatiale
CSR	Center for Space Research
ECMWF	European Centre for Medium-range Weather Forecasts
EOP	Earth orientation parameters
ERA-interim	ECMWF reanalysis (from January 1989 onward)
GAM	geodetic angular momentum
GAO	geodetic residuals GAM–AAM–OAM
GFZ	GeoForschungsZentrum
GIA	glacial isostatic adjustment
GNSS	Global navigation Satellite Systems
GPS	Global Positioning System
GRACE	Gravity Recovery and Climate Experiment
GSM	GRACE satellite-only model
GSMAM	GSM-based angular momentum
HAM	hydrological angular momentum
IERS	Rotation and Reference System Service

ITRF	International Terrestrial Reference Frame
ITSG	Institute of Theoretical Geodesy and Satellite Geodesy
JPL	Jet Propulsion Laboratory
LSDM	Land surface discharge model
MPIOM	Max Planck institute ocean model
OAM	oceanic angular momentum
OMCT	ocean model for circulation and tides
PM	polar motion
R ²	coefficient of determination
SLAM	sea-level angular momentum
SLR	satellite laser ranging
STD	standard deviation
STD _{diff}	standard deviation of differences
TUGO	Toulouse unstructured grid ocean
Var _{exp}	relative explained variance
VLBI	very long baseline interferometry

Appendix A

Table A1. Standard deviation of GAO and HAM time series for seasonal, non-seasonal, short-term (<730 days) non-seasonal, and long-term (>730 days) non-seasonal variation.

Series	Seasonal		Non-Seasonal		Non-Seasonal Short		Non-Seasonal Long	
	χ_R	χ_P	χ_R	χ_P	χ_R	χ_P	χ_R	χ_P
GAO	10.24	4.35	8.00	6.83	6.73	5.06	3.80	4.19
CSR RL05	3.29	3.08	8.20	7.37	4.32	4.83	6.72	4.98
CSR RL06	3.82	3.80	6.43	5.80	3.96	3.22	4.68	4.53
JPL RL05	4.95	4.69	11.83	6.49	9.20	4.34	6.82	4.15
JPL RL06	3.14	3.00	6.35	5.69	4.12	3.48	4.29	4.09
GFZ RL05	3.31	2.77	8.68	8.76	5.80	5.35	6.31	6.25
GFZ RL06	2.36	2.42	5.96	6.05	4.57	3.49	3.55	4.48
CNES/GRGS RL03	2.73	2.22	8.12	7.71	4.66	5.10	6.54	5.15
CNES/GRGS RL04	2.86	2.64	7.15	6.13	4.37	3.98	5.44	4.19
ITSG-Grace2016	2.48	1.94	9.02	6.94	6.75	3.86	5.68	5.15
ITSG-Grace2018	2.95	3.14	5.65	5.84	3.29	3.47	4.35	4.38
LSDM	6.75	2.72	7.20	6.61	2.79	2.13	6.45	5.97

Table A2. Correlation coefficients of χ_R and χ_P parts of seasonal variation between GAO and HAM computed from GRACE solutions and LSDM model, the percentage of variance in GAO explained by HAM functions, standard deviation (STD) of differences between GAO and HAM, and coefficient of determination (R²). The critical value of the correlation coefficient for 25 independent points and a confidence level of 0.95 was 0.34. The standard error of the difference between two correlation coefficients for 25 independent points was 0.30.

Series	Correlation Coefficient		Relative Explained Variance (%)		STD of Differences (mas)		R ²	
	χ_R	χ_P	χ_R	χ_P	χ_R	χ_P	χ_R	χ_P
CSR RL05	0.84	0.48	43	18	7.70	3.93	0.70	0.23
CSR RL06	0.87	0.62	51	32	7.18	3.60	0.75	0.38
JPL RL05	-0.57	0.31	-78	-50	13.68	5.33	0.32	0.09
JPL RL06	-0.07	0.08	-13	-37	10.91	5.09	0.00	0.01
GFZ RL05	0.67	0.40	33	11	8.39	4.11	0.45	0.16
GFZ RL06	0.84	0.58	34	34	8.35	3.54	0.71	0.34
CNES/GRGS RL03	0.63	0.74	27	49	8.78	3.10	0.40	0.54
CNES/GRGS RL04	0.60	0.73	26	52	8.82	3.03	0.36	0.53
ITSG-Grace2016	0.80	0.28	33	5	8.38	4.24	0.65	0.08
ITSG-Grace2018	0.68	0.64	31	41	8.53	3.34	0.46	0.42
LSDM	0.74	0.11	54	-25	6.93	4.86	0.55	0.01

Table A3. Correlation coefficients of χ_R and χ_P parts of non-seasonal variation between GAO and HAM computed from GRACE solutions and LSDM, the percentage of variance in GAO explained by HAM functions, standard deviation (STD) of differences between GAO and HAM, and coefficient of determination (R^2). The critical value of the correlation coefficient for 25 independent points and a confidence level of 0.95 was 0.34. The standard error of the difference between two correlation coefficients for 25 independent points was 0.30.

Series	Correlation Coefficient		Relative Explained Variance (%)		STD of Differences (mas)		R^2	
	χ_R	χ_P	χ_R	χ_P	χ_R	χ_P	χ_R	χ_P
CSR RL05	0.50	0.51	−3	−6	8.11	7.04	0.25	0.26
CSR RL06	0.66	0.68	42	44	6.12	5.11	0.44	0.47
JPL RL05	0.45	0.56	−87	16	10.94	6.25	0.20	0.31
JPL RL06	0.50	0.35	16	−12	7.33	7.21	0.25	0.12
GFZ RL05	0.42	0.67	−26	8	8.97	6.56	0.18	0.45
GFZ RL06	0.30	0.48	−11	7	8.41	6.58	0.09	0.23
CNES/GRGS RL03	0.49	0.53	−4	−8	8.15	7.10	0.24	0.28
CNES/GRGS RL04	0.48	0.56	6	21	7.75	6.09	0.23	0.32
ITSG–Grace2016	0.49	0.57	−15	13	8.60	6.36	0.24	0.33
ITSG–Grace2018	0.64	0.59	40	28	6.20	5.80	0.40	0.35
LSDM	0.35	0.64	−19	29	8.72	5.74	0.12	0.40

Table A4. Correlation coefficients of χ_R and χ_P parts of short-term (<730 days) non-seasonal variation between GAO and HAM computed from GRACE solutions and LSDM model, the percentage of variance in GAO explained by HAM functions, standard deviation (STD) of differences between GAO and HAM, and coefficient of determination (R^2). The critical value of the correlation coefficient for 25 independent points and a confidence level of 0.95 was 0.34. The standard error of the difference between two correlation coefficients for 25 independent points was 0.30.

Series	Correlation Coefficient		Relative Explained Variance (%)		STD of Differences (mas)		R^2	
	χ_R	χ_P	χ_R	χ_P	χ_R	χ_P	χ_R	χ_P
CSR RL05	0.46	0.37	18	−20	6.09	5.54	0.21	0.14
CSR RL06	0.64	0.54	40	29	5.21	4.28	0.40	0.29
JPL RL05	0.32	0.37	−99	−11	9.50	5.33	0.10	0.13
JPL RL06	0.25	−0.10	−6	−60	6.94	6.41	0.06	0.01
GFZ RL05	0.34	0.65	−16	25	7.24	4.39	0.12	0.42
GFZ RL06	0.28	0.20	−8	−19	6.98	5.53	0.08	0.04
CNES/GRGS RL03	0.30	0.41	−6	−20	6.93	5.54	0.09	0.16
CNES/GRGS RL04	0.30	0.38	−4	−2	6.86	5.12	0.09	0.14
ITSG–Grace2016	0.38	0.45	−24	11	7.50	4.79	0.14	0.20
ITSG–Grace2018	0.56	0.49	31	20	5.60	4.52	0.31	0.24
LSDM	0.26	0.45	5	20	6.57	4.53	0.07	0.20

Table A5. Correlation coefficients of χ_R and χ_P parts of long-term (>730 days) non-seasonal variation between GAO and HAM computed from GRACE solutions and LSDM model, the percentage of variance in GAO explained by HAM functions, standard deviation (STD) of differences between GAO and HAM, and coefficient of determination (R^2). The critical value of the correlation coefficient for 25 independent points and a confidence level of 0.95 was 0.34. The standard error of the difference between two correlation coefficients for 25 independent points was 0.30.

Series	Correlation Coefficient		Relative Explained Variance (%)		STD of Differences (mas)		R^2	
	χ_R	χ_P	χ_R	χ_P	χ_R	χ_P	χ_R	χ_P
CSR RL05	0.69	0.65	−69	12	4.94	3.92	0.47	0.42
CSR RL06	0.76	0.81	35	57	3.04	2.73	0.58	0.65
JPL RL05	0.72	0.74	−65	48	4.88	3.02	0.51	0.54
JPL RL06	0.87	0.71	69	44	2.10	3.12	0.76	0.51
GFZ RL05	0.64	0.82	−64	21	4.81	3.65	0.41	0.67
GFZ RL06	0.50	0.74	6	43	3.45	3.15	0.25	0.54
CNES/GRGS RL03	0.84	0.60	−7	−3	3.88	4.24	0.71	0.36
CNES/GRGS RL04	0.86	0.72	40	44	2.90	3.13	0.74	0.52
ITSG–Grace2016	0.79	0.73	13	28	3.54	3.54	0.62	0.53
ITSG–Grace2018	0.85	0.67	64	32	2.26	3.45	0.73	0.45
LSDM	0.60	0.86	−86	43	5.15	3.13	0.36	0.75

Table A6. Background models and data sources of temporal GRACE gravity field models *. ECMWF, European Centre for Medium-Range Weather Forecasts; ERA, ECMWF reanalysis.

Temporal Gravity Field Model	Mean Gravity Field Model	N Body Perturbations	Pole Tides	Ocean Tides	Atmospheric and Oceanic Non-Tidal Mass Variations	Data Source	Reference
CSR RL05	GIF48	DE 405	IERS 2010 (cubic)	GOT4.8	AOD1B RL05	https://podaac-tools.jpl.nasa.gov/drive/files/GeodeticsGravity/grace/L2	[42]
CSR RL06	GGM05C	DE 430	IERS 2010 (linear)	GOT4.8	AOD1B RL06	https://podaac-tools.jpl.nasa.gov/drive/files/GeodeticsGravity/grace/L2	[43]
JPL RL05	GIF48	DE 421	IERS 2010 (cubic)	GOT4.7	AOD1B RL05	https://podaac-tools.jpl.nasa.gov/drive/files/GeodeticsGravity/grace/L2	[44]
JPL RL06	GGM05C	DE 430	IERS 2010 (linear)	FES2014b	AOD1B RL06	https://podaac-tools.jpl.nasa.gov/drive/files/GeodeticsGravity/grace/L2	[45]
GFZ RL05	EIGEN-6C	DE 421	Constant mean pole	EOT11a	AOD1B RL05	https://podaac-tools.jpl.nasa.gov/drive/files/GeodeticsGravity/grace/L2	[46]
GFZ RL06	EIGEN-6C4	DE 430	IERS 2010 (linear)	FES2014	AOD1B RL06	https://podaac-tools.jpl.nasa.gov/drive/files/GeodeticsGravity/grace/L2	[47]
CNES/GRGS RL03	EIGEN-GRGS.RL03-v2.MEAN-FIELD	DE 405	IERS 2010 (cubic)	FES2012	ECMWF ERA-Interim (atmosphere) + TUGO (ocean)	http://grgs.obs-mip.fr/grace	[48]
CNES/GRGS RL04	EIGEN-GRGS.RL03-v2.MEAN-FIELD	DE 405	IERS 2010 (linear)	FES2014	ECMWF ERA-Interim (atmosphere) + TUGO (ocean)	http://grgs.obs-mip.fr/grace	[49]
ITSG-Grace2016	GOCO04s	DE 421	IERS 2010 (cubic)	EOT11a	AOD1B RL05	http://icgem.gfz-potsdam.de/series	[50]
ITSG-Grace2018	ITSG-GraceGoce2017	DE 421	IERS 2010 (linear)	FES2014b + GRACE	AOD1B RL06 + LSDM	http://icgem.gfz-potsdam.de/series	[51]

* Solid Earth tides for all solutions were based on the Rotation and Reference System Service (IERS) 2010 conventions (Petit and Luzum, 2010) [69].

References

1. Lambeck, K. *The Earth's Variable Rotation: Geophysical Causes and Consequences*; Cambridge University Press: Cambridge, UK, 1980.
2. Brzeziński, A.; Nastula, J.; Kołaczek, B.; Ponte, R.M. Oceanic excitation of polar motion from interannual to decadal periods. In Proceedings of the International Association of Geodesy, IAG General Assembly, Sapporo, Japan, 30 June–11 July 2003.
3. Brzeziński, A.; Nastula, J.; Kołaczek, B. Seasonal excitation of polar motion estimated from recent geophysical models and observations. *J. Geodyn.* **2009**, *48*, 235–240. [[CrossRef](#)]
4. Gross, R.S.; Fukumori, I.; Menemenlis, D. Atmospheric and oceanic excitation of the Earth's wobbles during 1980–2000. *J. Geophys. Res. Solid Earth.* **2003**, *108*, 2370. [[CrossRef](#)]
5. Nastula, J.; Ponte, R.M. Further evidence for oceanic excitation of polar motion. *Geophys. J. Int.* **1999**, *139*, 123–130. [[CrossRef](#)]
6. Nastula, J.; Ponte, R.M.; Salstein, D.A. Regional signals in atmospheric and oceanic excitation of polar motion. In *Polar Motion: Historical and Scientific Problems*; Dick, S., McCarthy, D., Luzum, B., Eds.; ASP: San Francisco, CA, USA, 2000; pp. 463–472. ISBN 1-58381-039-0.
7. Nastula, J.; Ponte, R.M.; Salstein, D.A. Comparison of polar motion excitation series derived from GRACE and from analyses of geophysical fluids. *Geophys Res Lett.* **2007**, *34*, 2–7. [[CrossRef](#)]
8. Nastula, J.; Salstein, D.A.; Kołaczek, B. Patterns of atmospheric excitation functions of polar motion from high-resolution regional sectors. *J. Geophys. Res.* **2009**, *114*, B04407. [[CrossRef](#)]
9. Nastula, J.; Pasnicka, M.; Kołaczek, B. Comparison of the geophysical excitations of polar motion from the period 1980.0–2007.0. *Acta Geophys.* **2011**, *59*, 561–577. [[CrossRef](#)]
10. Nastula, J.; Wińska, M.; Śliwińska, J.; Salstein, D. Hydrological signals in polar motion excitation—Evidence after fifteen years of the GRACE mission. *J. Geodyn.* **2019**, *124*, 119–132. [[CrossRef](#)]
11. Seoane, L.; Nastula, J.; Bizouard, C.; Gambis, D. Hydrological excitation of polar motion derived from GRACE gravity field solutions. *Int. J. Geophys.* **2011**, *2011*, 1–11. [[CrossRef](#)]
12. Śliwińska, J.; Wińska, M.; Nastula, J. Terrestrial water storage variations and their effect on polar motion. *Acta Geophys.* **2019**, *67*, 17–39. [[CrossRef](#)]
13. Wińska, M.; Nastula, J.; Kołaczek, B. Assessment of the global and regional land hydrosphere and its impact on the balance of the geophysical excitation function of polar motion. *Acta Geophys.* **2016**, *64*, 1–23. [[CrossRef](#)]
14. Wińska, M.; Nastula, J.; Salstein, D.A. Hydrological excitation of polar motion by different variables from the GLDAS model. *J. Geodesy.* **2017**, *17*, 7110. [[CrossRef](#)]
15. Wińska, M.; Śliwińska, J. Assessing hydrological signal in polar motion from observations and geophysical models. *Stud. Geophys. Et Geod.* **2019**, *63*, 95–117. [[CrossRef](#)]
16. Güntner, A. Improvement of global hydrological models using GRACE data. *Surv. Geophys.* **2008**, *29*, 375–397. [[CrossRef](#)]
17. Gross, R.S.; Chao, B.F. The rotational and gravitational signature of the December 26, 2004 Sumatran earthquake. *Surv. Geophys.* **2006**, *27*, 615–632. [[CrossRef](#)]
18. Greiner-Mai, H.; Jochmann, H.; Barthelmes, F. Influence of possible inner-core motions on the polar motion and the gravity field. *Phys. Earth Planet. Int.* **2000**, *117*, 81–93. [[CrossRef](#)]
19. Tapley, B.; Watkins, M.M.; Flechtner, F.; Reigber, C.; Bettadpur, S.; Rodell, M.; Famiglietti, J.; Landerer, F.; Chambers, D.; Reager, J.; et al. Contributions of GRACE to understanding climate change. *Nat. Clim. Chang.* **2019**, *9*, 358–369. [[CrossRef](#)] [[PubMed](#)]
20. Gross, R. Theory of earth rotation variations. In *VIII Hotine-Marussi Symposium on Mathematical Geodesy*; Sneeuw, N., Novák, P., Crespi, M., Sansò, F., Eds.; Springer: Cham, Switzerland, 2015; p. 142.
21. Chambers, D.P.; Wahr, J.; Nerem, R.S. Preliminary observations of global ocean mass variations with GRACE. *Geophys. Res. Lett.* **2004**, *31*, 1–4. [[CrossRef](#)]
22. Han, S.C.; Shum, C.K.; Bevis, M.; Ji, C.; Kuo, C.Y. Crustal dilatation observed by GRACE after the 2004 Sumatra–Andaman earthquake. *Science* **2006**, *313*, 658–662. [[CrossRef](#)]
23. Göttl, F.; Schmidt, M.; Seitz, F. Mass-related excitation of polar motion: An assessment of the new RL06 GRACE gravity field models. *Earth Planets Space* **2018**, *70*, 195. [[CrossRef](#)]

24. Śliwińska, J.; Wińska, M.; Nastula, J. Comparison of geodetic hydrological excitation functions with new GRACE RL06 solutions and hydrological excitations. In Proceedings of the AGU Fall Meeting 2018, Washington, DC, USA, 10–14 December 2018.
25. Śliwińska, J.; Nastula, J. Polar motion excitation functions from GRACE RL05 and RL06 solutions. In Proceedings of the IUGG General Assembly 2019, Montreal, QC, Canada, 8–18 July 2019.
26. Dobsław, H.; Dill, R.; Grötzsch, A.; Brzeziński, A.; Thomas, M. Seasonal polar motion excitation from numerical models of atmosphere, ocean, and continental hydrosphere. *J. Geophys. Res.* **2010**, *115*, B10. [[CrossRef](#)]
27. Seoane, L.; Nastula, J.; Bizouard, C.; Gambis, D. The use of gravimetric data from GRACE mission in the understanding of polar motion variations. *Geophys. J. Int.* **2009**, *178*, 614–622. [[CrossRef](#)]
28. Munk, W.H.; MacDonald, G. *The rotation of the Earth*; Cambridge University Press: Cambridge, UK, 1960.
29. Bizouard, C. Elliptic polarisation of the polar motion excitation. *J. Geod.* **2016**, *90*, 179–188. [[CrossRef](#)]
30. Smith, S.W. *Digital Signal Processing. A Practical Guide for Engineers and Scientists*; Elsevier Science Publishing Co Inc.: Oxford, UK, 2002. [[CrossRef](#)]
31. Brzeziński, A. Polar motion excitation by variations of the effective angular momentum function: Considerations concerning deconvolution problem. *Manuscr. Geod.* **1992**, *17*, 3–20.
32. Eubanks, T.M. Variations in the orientation of the Earth. In *Contributions of Space Geodesy to Geodynamics: Earth Dynamics: Geodynamic Series*; Smith, D.E., Turcotte, D.L., Eds.; American Geophysical Union: Washington, DC, USA, 1993; Volume 24, pp. 1–54.
33. Bizouard, C.; Lambert, S.; Gattano, C.; Becker, O.; Richard, J.Y. The IERS EOP 14C04 solution for Earth orientation parameters consistent with ITRF 2014. *J. Geod.* **2018**, *93*, 621. [[CrossRef](#)]
34. Altamimi, Z.; Rebischung, P.; Métivier, L.; Collilieux, X. ITRF2014: A new release of the International Terrestrial Reference Frame modeling nonlinear station motions. *J. Geophys. Res. Solid Earth* **2016**, *121*, 6109–6131. [[CrossRef](#)]
35. Dill, R.; Dobsław, H. Seasonal Variations in Global Mean Sea-Level and Consequences on the Excitation of Length-of-Day Changes. *Geophys. J. Int.* **2019**, *218*, 801–816. [[CrossRef](#)]
36. Naito, I.; Zhou, Y.-H.; Sugi, M.; Kawamura, R.; Sato, N. Three-dimensional Atmospheric Angular Momentum Simulated by the Japan Meteorological Agency model for the period of 1955–1994. *J. Meteorol. Soc. Jpn.* **2000**, *78*, 111–122. [[CrossRef](#)]
37. Zhou, Y.H.; Chen, J.L.; Liao, X.H.; Wilson, C.R. Oceanic excitations on polar motion: A cross comparison among models. *Geophys. J. Int.* **2005**, *162*, 390–398. [[CrossRef](#)]
38. Vondrak, J.; Ron, C. Geophysical fluids, geomagnetic jerks, and their impact on Earth orientation. *Publ. Astron. Obs. Belgrade* **2017**, *96*, 51–60.
39. Dobsław, H.; Bergmann-Wolf, I.; Dill, R.; Poropat, L.; Flechtner, F. Product description document for AOD1B release 06. Technical report GRACE, 327–750. Available online: [Ftp://isdcdftp.gfz-potsdam.de/grace/DOCUMENTS/Level-1/GRACE_AOD1B_Product_Description_Document_for_RL06.pdf](http://isdcdftp.gfz-potsdam.de/grace/DOCUMENTS/Level-1/GRACE_AOD1B_Product_Description_Document_for_RL06.pdf) (accessed on 24 September 2019).
40. Dobsław, H.; Wolf, I.; Dill, R.; Poropat, L.; Thomas, M.; Dahle, C.; Esselborn, S.; König, R.; Flechtner, F. A new high-resolution model of non-tidal atmosphere and ocean mass variability for de-aliasing of satellite gravity observations: AOD1B RL06. *Geophys. J. Int.* **2017**, *211*, 263–269. [[CrossRef](#)]
41. Jungclauss, J.H.; Fischer, N.; Haak, H.; Lohmann, K.; Marotzke, J.; Matei, D.; Mikolajewicz, U.; Notz, D.; vonStorch, J.S. Characteristics of the ocean simulations in MPIOM, the ocean component of the MPI-Earth system model. *J. Adv. Model. Earth Syst.* **2013**, *5*, 422–446. [[CrossRef](#)]
42. Bettadpur, S. UTCSR level-2 Processing Standards Document for Level-2 Product Release 0005. Technical Report GRACE 2012. pp. 327–742. Available online: [Ftp://podaac-ftp.jpl.nasa.gov/allData/grace/docs/L2-CSR0005_ProcStd_v4.0.pdf](http://podaac-ftp.jpl.nasa.gov/allData/grace/docs/L2-CSR0005_ProcStd_v4.0.pdf) (accessed on 24 September 2019).
43. Bettadpur, S. UTCSR level-2 Processing Standards Document for Level-2 Product Release 0006. Technical Report GRACE 2018. pp. 327–742. Available online: [Ftp://podaac-ftp.jpl.nasa.gov/allData/grace/docs/L2-CSR006_ProcStd_v5.0.pdf](http://podaac-ftp.jpl.nasa.gov/allData/grace/docs/L2-CSR006_ProcStd_v5.0.pdf) (accessed on 24 September 2019).
44. Watkins, M.M.; Yuan, D. JPL level-2 Processing Standards Document for Level-2 Product Release 05.1. Technical Report GRACE. pp. 327–744. Available online: [Ftp://podaac-ftp.jpl.nasa.gov/allData/grace/docs/L2-JPL_ProcStd_v5.1.pdf](http://podaac-ftp.jpl.nasa.gov/allData/grace/docs/L2-JPL_ProcStd_v5.1.pdf) (accessed on 24 September 2019).

45. Yuan, D. JPL level-2 Processing Standards Document for Level-2 Product Release 06. Technical Report GRACE. pp. 327–744. Available online: [Ftp://podaac--ftp.jpl.nasa.gov/allData/grace/docs/L2--JPL_ProcStds_v6.0.pdf](ftp://podaac--ftp.jpl.nasa.gov/allData/grace/docs/L2--JPL_ProcStds_v6.0.pdf) (accessed on 24 September 2019).
46. Dahle, C.; Flechtner, F.; Gruber, C.; König, D.; König, R.; Michalak, G.; Neumayer, K.H. GFZ GRACE Level-2 Processing Standards Document for Level-2 Product Release 0005. Scientific Technical Report STR12/02–Data, Revised Edition. January 2013. Available online: http://icgem.gfz-potsdam.de/L2-GFZ_ProcStds_0005_v1.1-1.pdf (accessed on 24 September 2019).
47. Dahle, C.; Flechtner, F.; Murböck, M.; Michalak, G.; Neumayer, H.; Abrykosov, O.; Reinhold, A.; König, R. GFZ Level-2 Processing Standards Document for Level-2 Product Release 06. Scientific Technical Report STR-Data. 2019. Available online: [Ftp://podaac.jpl.nasa.gov/GeodeticsGravity/grace/docs/L2-GFZ_ProcStds_RL06_DRAFT.pdf](ftp://podaac.jpl.nasa.gov/GeodeticsGravity/grace/docs/L2-GFZ_ProcStds_RL06_DRAFT.pdf) (accessed on 24 September 2019).
48. Lemoine, J.-M.; Bourgoigne, S.; Bruinsma, S.; Gégout, P.; Reinquin, F.; Biancale, R. GRACE RL03–v2 monthly time series of solutions from CNES/GRGS/GRGS. In Proceedings of the 17th EGU General Assembly, Vienna, Austria, 12–17 April 2018.
49. Lemoine, J.-M.; Bourgoigne, S.; Biancale, R.; Gégout, P. The new GRGS–RL04 series of mass variations modelled with GRACE data. In Proceedings of the 20th EGU General Assembly, Vienna, Austria, 4–13 April 2018.
50. Mayer-Gürr, T.; Behzadpour, S.; Ellmer, M.; Kvas, A.; Klinger, B.; Zehentner, N. ITSG–Grace2016—Monthly and Daily Gravity Field Solutions from GRACE. GFZ Data Services. Available online: <http://dataservices.gfz-potsdam.de/icgem/showshort.php?id=escidoc:1697893> (accessed on 24 September 2019). [CrossRef]
51. Mayer-Gürr, T.; Behzadpour, S.; Ellmer, M.; Kvas, A.; Klinger, B.; Strasser, S.; Zehentner, N. ITSG–Grace2018—Monthly, Daily and Static Gravity Field Solutions from GRACE. GFZ Data Services. Available online: <http://dataservices.gfz-potsdam.de/icgem/showshort.php?id=escidoc:3600910> (accessed on 24 September 2019).
52. Dill, R. Hydrological Model LSDM for Operational Earth Rotation and Gravity Field Variations. GFZ Scientific Technical Report STR; 08/09. Available online: <http://gfzpublic.gfz-potsdam.de/pubman/item/escidoc:8770> (accessed on 24 September 2019).
53. Dill, R. Hydrological induced Earth rotation variations from standalone and dynamically coupled simulations. In Proceedings of the Journées 2008 Systèmes de Référence Spatio-Temporels, Dresden, Germany, 22–24 September 2008.
54. Dobsław, H.; Dill, R. Effective Angular Momentum Functions From Earth System Modelling at GeoForschungsZentrum in Potsdam. Technical Report, Revision 1.1 (March 18, 2019), GFZ Potsdam, Germany. Available online: <http://rz--vm115.gfz--potsdam.de:8080/repository/entry/show?entryid=e8e59d73--c0c2-4a9d--b53b--f2cd70f85e28> (accessed on 24 September 2019).
55. Dobsław, H.; Dill, R. Predicting Earth Orientation Changes from Global Forecasts of Atmosphere–Hydrosphere Dynamics. *Adv. Space Res.* **2018**, *61*, 1047–1054. [CrossRef]
56. Otnes, K.; Enochson, L. *Digital Time Series Analysis*; Wiley: New York, NY, USA, 1972.
57. Youm, K.; Seo, K.W.; Jeon, T.; Na, S.H.; Chen, J.; Wilson, C.R. Ice and groundwater effects on long term polar motion (1979–2010). *J. Geodyn.* **2017**, *106*, 66–73. [CrossRef]
58. Adhikari, S.; Ivins, E.R. Climate–driven polar motion: 2003–2015. *Sci. Adv.* **2016**. [CrossRef] [PubMed]
59. Adhikari, S.; Caron, L.; Steinberger, B.; Reager, J.T.; Kjeldsen, K.K.; Marzeion, B.; Larour, E.; Ivins, E.R. What drives 20th century polar motion? *Earth Planet. Sci. Lett.* **2018**, *502*, 126–132. [CrossRef]
60. Kuang, W.; Chao, B.F.; Chen, J. Decadal polar motion of the Earth excited by the convective outer core from geodynamo simulations. *J. Geophys. Res. Solid Earth* **2017**, *122*, 8459–8473. [CrossRef]
61. Dumberry, M.; Bloxham, J. Inner core tilt and polar motion. *Geophys. J. Int.* **2002**, *151*, 377–392. [CrossRef]
62. Greiner–Mai, H.; Barthelmes, F. Relative wobble of the Earth’s inner core derived from polar motion and associated gravity variations. *Geophys. J. Int.* **2001**, *144*, 27–36. [CrossRef]
63. Chen, J.L.; Wilson, C.R.; Zhou, Y.H. Seasonal excitation of polar motion. *J. Geodyn.* **2012**, *62*, 8–15. [CrossRef]
64. Nastula, J.; Śliwińska, J. Estimating hydrological signal in polar motion from new GRACE RL06 solutions. In Proceedings of the IUGG General Assembly 2019, Montreal, QC, Canada, 8–18 July 2019.
65. De Viron, O.; Panet, I.; Diament, M. Extracting low frequency climate signal from GRACE data. *eEarth* **2006**, *1*, 9–14. [CrossRef]

66. Gille, S. UCSD-MAE 127: Statistical Methods for Environmental Sciences and Engineering, Lecture 10, University of California, San Diego, La Jolla, The United States. 2005. Available online: <http://pordlabs.ucsd.edu/sgille/mae127/lecture10.pdf> (accessed on 24 September 2019).
67. Moriasi, D.N.; Arnold, J.G.; Van Liew, M.W.; Bingner, R.L.; Harmel, R.D.; Veith, T.L. Model evaluation guidelines for systematic quantification of accuracy in watershed simulations. *Trans. ASABE* **2007**, *50*, 885–900. [[CrossRef](#)]
68. Meyrath, T.; van Dam, T. A comparison of interannual hydrological polar motion excitation from GRACE and geodetic observations. *J. Geodyn.* **2016**, *99*, 1–9. [[CrossRef](#)]
69. Petit, G.; Luzum, B. IERS Conventions. Technical Report IERS Technical Note no. 36, Verlag des Bundesamts für Kartographie und Geodäsie, Frankfurt am Main, Germany. 2010. Available online: <https://www.iers.org/IERS/EN/Publications/TechnicalNotes/tn36.html> (accessed on 24 September 2019).
70. Wahr, J.; Nerem, R.S.; Bettadpur, S. The pole tide and its effect on GRACE time-variable gravity measurements: Implications for estimates of surface mass variations. *J. Geophys. Res. Solid Earth* **2015**, *120*, 4597–4615. [[CrossRef](#)]
71. Dobslaw, H.; Flechtner, F.; Bergmann-Wolf, I.; Dahle, C.; Dill, R.; Esselborn, S.; Sasgen, I.; Thomas, M. Simulating high-frequency atmosphere-ocean mass variability for de-aliasing of satellite gravity observations: AOD1B RL05. *J. Geophys. Res.* **2013**, *118*, 3704–3711. [[CrossRef](#)]
72. Gross, R.S. An improved empirical model for the effect of long-period ocean tides on polar motion. *J. Geod.* **2009**, *83*, 635–644. [[CrossRef](#)]
73. Gross, R.S. The effect of ocean tides on the Earth's rotation as predicted by the results of an ocean tide model. *Geophys. Res. Lett.* **1993**, *20*, 293–296. [[CrossRef](#)]



© 2020 by the authors. Licensee MDPI, Basel, Switzerland. This article is an open access article distributed under the terms and conditions of the Creative Commons Attribution (CC BY) license (<http://creativecommons.org/licenses/by/4.0/>).